3-6-2006

Prediction of Flight-Level Radiation Hazards Due To Solar Energetic Protons

Matthew P. Sattler

Follow this and additional works at: https://scholar.afit.edu/etd

Part of the The Sun and the Solar System Commons

PREDICTION OF FLIGHT-LEVEL RADIATION HAZARDS DUE TO SOLAR

ENERGETIC PROTONS

THESIS

Matthew P. Sattler, Captain, USAF

AFIT/GAP/ENP/06-16

DEPARTMENT OF THE AIR FORCE
AIR UNIVERSITY

AIR FORCE INSTITUTE OF TECHNOLOGY

Wright-Patterson Air Force Base, Ohio

PREDICTION OF FLIGHT-LEVEL RADIATION HAZARDS DUE TO SOLAR

ENERGETIC PROTONS

THESIS

Presented to the Faculty

Department of Engineering Physics

Graduate School of Engineering and Management

Air Force Institute of Technology

Air University

Air Education and Training Command

In Partial Fulfillment of the Requirements for the

Degree of Master of Science (Applied Physics)

Matthew P. Sattler, B.S.

Captain, USAF

January 2006

PREDICTION OF FLIGHT-LEVEL RADIATION HAZARDS DUE TO SOLAR

ENERGETIC PROTONS

Matthew P. Sattler, B.S.
Captain, USAF

Approved:

_____
Christopher Smithtro (Chairman)

6 Mar 06
date

_____
David Gerts (Member)

6 Mar 06
date

_____
Thomas Niday (Member)

6 Mar 06
date

AFIT/GAP/ENP/06-16

Abstract

The radiation environment at aircraft altitudes is caused primarily by high-energy particles originating from outside the near-earth environment. These particles generally come from outside our solar system and are called galactic cosmic rays. Occasionally however, a transient solar event will also accelerate energetic protons toward the earth. If these protons reach the upper atmosphere, they produce secondary particles via collisions, resulting in increased radiation levels in the atmosphere. Air crews and electronic systems flying at high altitudes during one of these events are subjected to these increased levels of radiation which can result in health problems for personnel and soft errors in electronics. Much work has been performed to calculate radiation dose rates at flight levels due to non-solar energetic particles, however very few dose rate measurements have been made shortly after the eruption of a large solar flare. Using energetic proton data measured at geosynchronous orbits and Monte Carlo transport codes, an attempt is made to estimate radiation dose rates at different altitudes and locations during solar events. The goal is to provide accurate information about the radiation environment at high altitudes, which will allow aircraft and personnel to avoid locations where health or the mission may be negatively impacted.

Acknowledgements

I would like to thank my thesis advisor, Major Christopher Smithtro, for his efforts and expertise throughout this thesis. His teaching style and sense of humor helped me keep a positive attitude and made learning fun. Major Smithtro is a fine example of what a military professional should be.

I would also like to thank Major David Gerts for his assistance in helping me to understand the assumptions and complications introduced by the various transport codes used to calculate dose rates. His discussions helped me gain focus and provided me with the necessary information to critically evaluate the different processes used in the calculations.

Finally, I would like to thank Dr. Herb Sauer from the Cooperative Institute for Research in Environmental Science (CIRES), and Prof. Kyle Copeland from the Civil Aerospace Medical Institute (CAMI) for their help and expertise given to me on the problem of determining dose rates due to solar protons.

Matthew P. Sattler

Table of Contents

List of Figures

List of Tables

PREDICTION OF FLIGHT-LEVEL RADIATION HAZARDS DUE TO SOLAR ENERGETIC PROTONS

I. Introduction

The earth is constantly bombarded by high-energy particles from space. Historically these particles were called galactic cosmic rays because they were thought to originate from deep space. It was discovered later that a small percentage actually originates from the sun during solar disturbances. All of these particles have the potential to do damage to both equipment and personnel. Fortunately, the earth's magnetic field and atmosphere both act as a shield to radiation originating from outside the terrestrial environment, preventing most of the harmful particles from reaching the surface. However, particles with enough energy can make their way through the magnetic field and penetrate deep into the atmosphere. As a result, aircraft pilots and personnel, and electronic systems aboard high-flying aircraft are constantly exposed to a higher level of ionizing radiation than that received by the general population and systems located at the earth's surface.

Ionizing radiation refers to energetic particles that interact with an atom and can strip electrons or even break up the nucleus. If this occurs in body tissues, it may result in health problems, and in electronics it can greatly increase the rate of single event upsets. The problem for electronics will only get worse as more low power, smaller sized electronic devices are used in future aircraft (4:81).

Although models currently exist to predict the levels of ionizing radiation due to galactic cosmic rays, there are very few methods that account for the occasional burst of solar energetic particles, and the methods that do exist have only come about in the past few years. The Air Force currently has no quantitative warning system in place to protect sensitive aircraft equipment and crew from these dangerous levels of radiation.

The main source of this hazardous radiation is galactic cosmic radiation. Galactic cosmic radiation is composed of high energy nuclei which are thought to propagate throughout all space unoccupied by dense matter. The origin of these particles is still a matter of debate, but theories indicate that it may have both galactic and extragalactic sources (5). Regardless of their origin, these particles range in energy from a few hundred MeV to 10^{11} GeV, and are often energetic enough to penetrate the earth's magnetic field and enter the atmosphere.

Data shows this galactic cosmic ray flux to be anti-correlated to the solar cycle, increasing in flux during solar minimum and decreasing in flux during solar maximum. During solar maximum, solar magnetic activity increases dramatically; this in turn causes many cosmic rays to be deflected before they can make their way through the heliosphere and to the earth's magnetic field (29). Thus we see a decrease in the galactic cosmic ray flux during solar maximum as shown in Figure 1 below.

The second type of radiation that must be considered is that produced by the sun. A solar flare or coronal mass ejection (CME) may accelerate high-energy protons toward the earth. If these particles reach the top of the atmosphere they will create a secondary particulate radiation via collisions. Aircraft and aircraft personnel are then subjected to

this secondary radiation flux which is a function of geographic position (minimum at the equator, maximum at the poles), altitude of the aircraft (minimum at lower altitudes, maximum at higher altitudes), and solar activity.
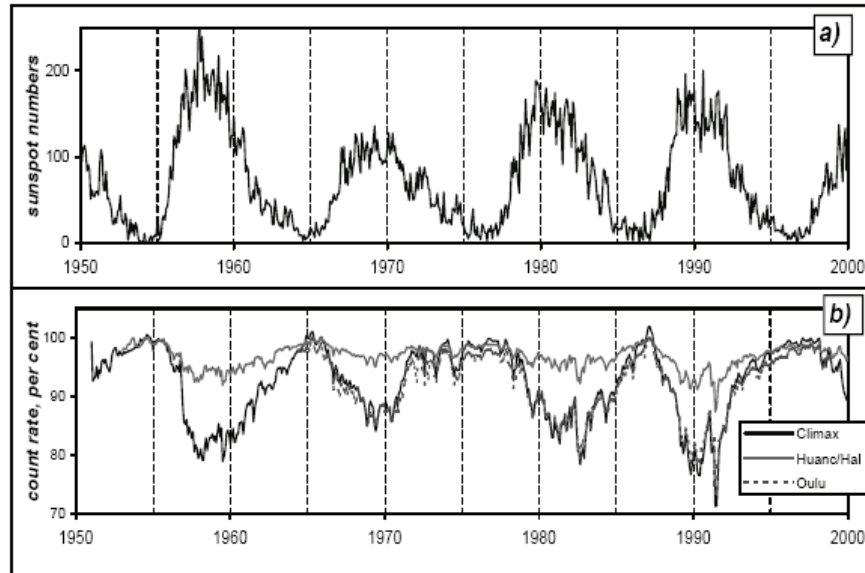
Figure 1: Panel a) shows solar activity levels as measured by sunspot numbers. Panel b) shows the galactic cosmic ray count as measured by three different neutron monitors. The inverse relationship between the two is due to increased magnetic activity during high solar activity, which causes incoming galactic cosmic rays to be deflected away from the heliosphere (11).

Radiation exposure is usually expressed in terms of effective dose, with units given in sieverts (Sv). A sievert is the SI unit of absorbed dose, and can be expressed as 1 joule/kilogram. Sometimes, harmful radiation exposure is expressed in units of rem (roentgen equivalent man), where 100 rem = 1 sievert.

The effects of ionizing radiation from the sun cannot be avoided by flying at night. Although high-energy particles from a severe solar disturbance may initially be anisotropic, the spreading effect by the interplanetary and the earth's magnetic fields eventually cause the incoming particle flux to be much more isotropic in nature (7:2).

Impact on Air Force Mission

Certain Air Force missions are extremely susceptible to high altitude radiation hazards. High altitude flyers – especially U2 pilots – fly at altitudes and latitudes where the atmosphere and magnetic field do not provide as much protection from the secondary particle flux generated by incoming galactic cosmic rays and energetic solar protons. Standard U2 operating altitudes are in excess of 80,000 ft (greater than 24 km) (36). During solar quiescent periods, a typical radiation dose rate received from galactic cosmic radiation at these altitudes is approximately 10 - 17 µSv/hr, or 0.010 - 0.017 mSv/hr. However, during a large solar proton event, it's possible for the radiation dose rates to increase to almost 200 µSv/hr, or 0.20 mSv/hr, with the increased rates due mostly to energetic solar protons (22).

Currently, the Air Force Weather Agency (AFWA) produces a product predicting radiation dose rates at specific altitudes using a model called CARI-6. This model is the latest in a series of computer programs whose purpose is to calculate the radiation dose accrued during an aircraft's flight. However, the CARI-6 model only takes into account radiation produced by galactic cosmic rays – increased radiation created by a solar energetic particle event is not factored into the radiation dose prediction. The CARI-6 model does account for solar activity by using an average monthly heliocentric potential. The heliocentric potential is an interplanetary magnetic field index. The more active the sun is, the stronger the interplanetary magnetic field, and thus the higher the heliocentric potential (11). This factor allows the CARI-6 model to account for increases and decreases in the galactic cosmic radiation incident at the top of the earth's atmosphere,

but it does not account for the occasional flare or CME which accelerates high-energy protons in the earth's direction.

Research Scope and General Approach

The goal of this effort is to determine the radiation dose rate at high altitudes due to solar energetic protons. This is a complex problem because of the transient and short-lived nature of solar proton events, and the complex nature of the earth's geomagnetic shielding.

Measurements of energetic protons are made by sensors onboard the National Oceanic and Atmospheric Administration's (NOAA) suite of geostationary weather satellites, called Geostationary Operational Environment Satellites (GOES). These measurements can be used to estimate the flux of energetic protons into the earth's magnetosphere. The flux is characterized by an energy spectrum, which can be used to estimate dose rates throughout the earth's atmosphere.

Along with studying the energy spectrum of incoming solar energetic particles and the calculation of dose rates, additional concepts such as rigidity and geomagnetic cutoff are described. These concepts are necessary to predict dose rates for locations around the earth.

Expected Results

The main focus of this study is the development of an algorithm to determine radiation dose rates at given altitudes and positions around the earth. We will also determine the role that the spectral hardness of the incoming proton spectrum plays in

determining the amount of radiation dose produced and the role that geomagnetic shielding plays in altering the dose rates. We attempt to determine which types of solar proton events are the most dangerous to aircraft and personnel, as well as the typical duration of these events. An evaluation of the current methods for modeling the spectrum of solar protons is also provided.

To accomplish this, Chapter II introduces background concepts necessary to understand the problem of radiation dose rates in the atmosphere. First, the radiation environment in the atmosphere is described, along with the effects of radiation, dose rates due to radiation, and how these are calculated. The different sources of radiation are discussed in Chapter II, along with the important concepts of rigidity and geomagnetic cutoff, which determine whether a particle will arrive at the top of the atmosphere. Next, the production of secondary particles which cause the bulk of the radiation dose is described, along with how these particles are transported through the atmosphere. Finally, the measurement of high-energy protons originating from the sun will be discussed.

Chapter III covers the methodologies used to come up with a solution to the problem. The method in which a complete particle spectrum is recreated from available measurements is discussed first, followed by the concept of spectral hardness. Then, the process by which dose rates in the atmosphere are calculated from the modeled spectrum is covered, along with several alternate methods to model the energy spectrum. The concept of geomagnetic cutoff rigidity is incorporated into the solution, and finally, the assumptions and known sources of error in these methodologies are discussed.

Chapter IV covers the results and analysis. Two historical events are analyzed and compared. Comparisons between results with and without geomagnetic cutoffs are made, along with results from other operational radiation dose rate models currently in use. Analysis of the two historical events will show that solar protons can produce significant levels of radiation at high altitudes for brief periods of time immediately following large solar flares or coronal mass ejections. Further, the results will show that geomagnetic effects must be taken into account to accurately predict radiation dose rates.

Finally, Chapter V contains a brief summary and conclusions drawn from the research, including the basic finding of this research, that short-lived spikes in radiation dose rates at high altitudes can be a significant source of an aircrew's annual radiation exposure. The paper will conclude with recommendations for future work.

II. Background

Chapter Overview

This chapter starts with background information regarding the radiation environment at high altitudes and how dose rates are measured and calculated. It then progresses to explain the types of radiation that contribute to the overall dose rates. Next, charged particle access to the atmosphere is described followed by a description of how the charged particles interact with the atmosphere to produce ionizing radiation. The concept of rigidity is introduced and finally, the process by which the energetic particles are measured at geosynchronous orbit is described.

The Radiation Environment at Aircraft Altitudes

The term 'aircraft altitudes' refers to the range of altitudes at which commercial airlines and Department of Defense aircraft fly. Typical operating altitudes for commercial airlines are generally 20,000 feet to 50,000 feet. Department of Defense and especially United States Air Force aircraft may fly much higher, with the operating altitude envelope extending upwards to 80,000 feet. Therefore, for the purposes of this study, aircraft altitudes refer to the range from 20,000 to 80,000 ft.

The radiation environment at these altitudes has a complex nature and is different from that on the ground. Its composition and strength depend on the properties of the primary cosmic ray and solar energetic particle flux and vary with altitude. The cosmic ray and solar energetic particle fluxes are modulated by solar activity and influenced by the earth's magnetic field. Both effects primarily alter the low-energy portion of the

spectrum – generally those particles with energies less than about 10 GeV (11). This low energy portion of the spectrum is responsible for most of the secondary particles reaching aircraft altitudes because of its large flux.

Radiation Effects and Dose Rate Calculations

Ionizing radiation refers to any form of energy that can strip electrons from their orbits, break chemical bonds, or contribute to changes in chemical properties. High-energy radiation can displace or fragment the nuclei of atoms, producing recoil or spallation products leading to a cascading effect of lower-level ionization up to several tens of μm around the 1 to 5 nm core of the primary particle's track. A typical human cell dimension is approximately 10 μm in diameter (35).

High energy cosmic rays affect tissues in the body differently than the lower energy radiation that most studies are based on. This is important because radiation effects must be understood in order to understand the risks of exposure to pilots, aircrews, and electronic systems flying at high altitudes. The cumulative effect of exposure to ionizing radiation is a function of several factors: the total dose received, the location and distribution of the dose, the rate of accumulation of the dose, and the types of radiation that produce the dose. The effects of ionizing radiation fall into two broad categories: prompt and delayed.

The prompt effects include dizziness, headaches, nausea, and may result in severe illness or death. Prompt effects, although extremely rare at any aircraft altitude, can have a serious impact on the ability of an aircrew to complete the mission. Measures must be developed and implemented to mitigate these effects.

Delayed effects are either nonstochastic (where the severity depends on the dose) or stochastic (where the probability of occurrence depends on the dose). Nonstochastic delayed effects include cataracts and nonmalignant skin damage. Stochastic delayed effects include induced cancer and genetic damage. Although delayed effects would not directly impact the immediate mission, the Air Force does have a responsibility to keep the overall risk to life as low as reasonably achievable. Precise risk/benefit assessments are up to commanders who need all the necessary information to make the decisions in the context of overall mission risk. It is important to remember that the impact of radiation exposure stays with a person for the rest of their life (35). The Federal Aviation Administration's recommended radiation exposure limit for an aircrew member is a 5-year average effective dose of 20 mSv per year, with no more than 50 mSv in a single year (7). The Air Force does not have established limits for radiation exposure, although such regulations are currently being developed (36).

As mentioned previously, the radiation impact to aircrews is measured in units of sieverts, and is called the effective dose. The effective dose is the sum of the weighted equivalent doses in all the tissues and organs of the body. It is given by the following expression:

$$E = \sum_{T} W_{T} H_{T} \, ,$$

(1)

where H is the equivalent dose in tissue T and W is the weighting factor for tissue T (17). The weighting factors for specific types of radiation are listed in Table 1 below.

The equivalent dose is related to the total absorbed dose by a factor that accounts for the relative cancer risk of primary and secondary particles. It is an attempt to

characterize different biological effects of different types of radiation using a single scale. The equivalent dose depends on the location within the body where the radiation is received, due to its self-shielding. This requires that it be calculated for several locations on the body, such as blood-forming organs, skin, eyes, breasts, and other organs and tissues (35).

Table 1: Radiation weighting factors for high energy radiation (17).

Radiation	Energy (GeV)	Radiation Weighting Factor
Neutrons	0.05 – 0.1	5
	0.1 – 0.5	4
	0.5 – 10	3
	>10	2
Protons	>0.01	2
Negative pions	<0.05	5
	≥0.05	2
Positive pions	<0.1	1
	≥0.1	2
Negative and positive muons	$10^{-3} - 10^{-4}$	1
Negative and positive kaons	$10^{-3} - 10^{-4}$	2

Conversion of observed particle fluxes to radiation dose rates is not straight-forward. The calculations require detailed information about the particle composition and energy spectrum, which will be discussed in Chapter III. The conversion of the particle flux to a dose rate requires the use of coefficients to estimate the radiation doses on each body part. These coefficients are calculated by irradiating a simulated body using broad parallel beams and fully isotropic radiation incidence. The beam directions are anterior-posterior (AP), posterior-anterior (PA), and right lateral (LAT). The isotropic (ISO) irradiation is calculated using an inward-directed, biased cosine source on

11

a spherical surface. These models are used later in Chapter III: Methodology to calculate

coefficients, which are necessary to estimate dose rates (17).

Galactic Cosmic Radiation

Galactic cosmic radiation is a term applied to the observed high-energy nuclei

believed to propagate throughout all space. The origin of these nuclei is still debated and

may be either galactic or extra-galactic or both. Outside the heliosphere, it is thought that

the galactic cosmic ray flux is isotropic. Measured anisotropies due to propagation

effects inside the heliosphere are approximately 1% (5).

The primary cosmic ray flux refers to those galactic cosmic rays that reach the

earth's atmosphere. The composition of this flux is approximately 83% protons, 13%

alpha particles, 1% nuclei of atomic number $Z > 2$, and 3% electrons. The energy

spectrum of the primary cosmic ray flux extends from a few hundred MeV to greater than

10^{11} GeV (5).

The differential energy spectra of all high-energy cosmic rays above

approximately 1 GeV/nucleon can be modeled using a power law in energy of the form

$$F(E) = kE^{-\gamma}, \tag{2}$$

where E is the kinetic energy per nucleon, and γ is the spectral index (5). The spectral

index is a measure of the hardness of the flux, and is sometimes referred to as the spectral

hardness. A flux with a larger number of high energy particles is said to be harder than a

flux with fewer high energy particles. Similarly, a flux with a larger number of low

energy particles is said to be softer than a flux with fewer low energy particles. This

12

concept is important because two measured fluxes may have the same total number of particles, but the harder flux will have a higher total energy content than the softer flux.

The differential spectrum of the primary cosmic ray flux deviates from the power law at energies below about 1 GeV/nucleon. At these lower energies, the spectrum changes with time, mostly as a result of the strength of the interplanetary magnetic field, which acts to modulate the galactic cosmic ray flux. Figure 2 below shows the primary cosmic ray differential energy spectrum for helium and hydrogen. The shaded areas are those regions where the spectrum deviates from the power law and is affected by the interplanetary magnetic field. The upper bound is a solar minimum spectrum; the lower bound is a solar maximum spectrum (5).

Galactic cosmic rays are influenced by the solar wind and the interplanetary magnetic field when entering the heliosphere. This influence, which can be detected in the cosmic ray intensities recorded at the earth, is called the solar (or heliospheric) modulation and, as previously mentioned, depends on the level of solar activity. During periods of high solar activity, the sun's magnetic complexity greatly increases, usually resulting in a stronger interplanetary magnetic field. A stronger magnetic field means the trajectories of energetic particles will be deflected more than usual, which results in a decrease in the primary cosmic ray flux. Thus, cosmic ray intensities measured at the earth are inversely related to the sunspot number, and the solar modulation of galactic cosmic rays takes on an 11-year cycle similar to the solar cycle (20).

This solar modulation does not extend across the entire range of cosmic ray energies, but rather is concentrated on the lower-energy range, usually below 10 GeV.

The trajectories of high energy protons (above 10 GeV) are bent significantly less than those of lower energy protons (below 1 GeV). Therefore, the higher energy cosmic rays are less affected by changes in the solar output. For the lower energy cosmic rays, the effect is significant even during solar minimum when the modulation is weaker (11). At 100 MeV per nucleon, the particle fluxes differ by a factor of 10 between maximum and minimum solar activity conditions, whereas at 4 GeV only a variation of about 20% is observed (20). At energies above 50 GeV, energetic particles are not affected by solar modulation (21). More than 80% of the radiation dose due to galactic cosmic rays at aircraft altitudes is caused by cosmic rays with energies below 100 GeV (21).
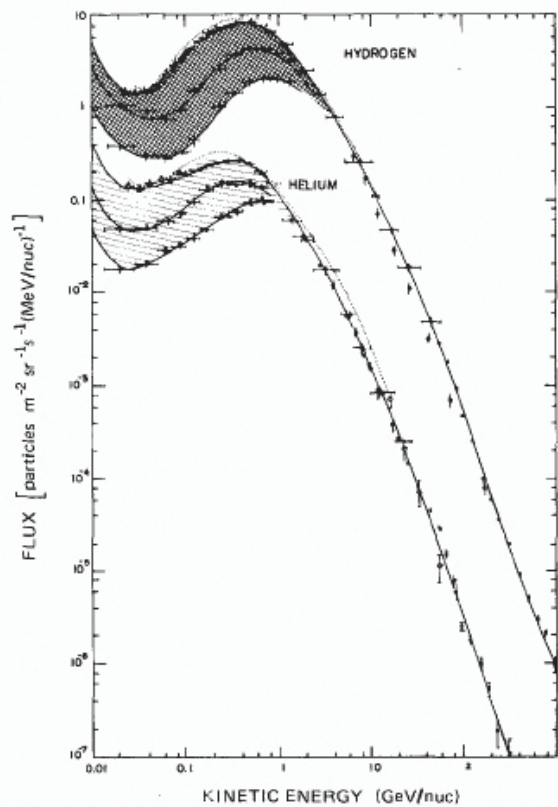
Figure 2: Primary cosmic ray differential energy spectra for helium and hydrogen shown on a log scale. The shaded areas are those regions where the spectra deviate from the power law and are affected by solar activity. The upper/lower bound is a solar minimum/maximum spectrum. The hydrogen spectrum has been multiplied by a factor of five so the lower portion of the spectrum avoids merging with the top of the helium spectrum (26:6-4).

14

Cosmic ray intensities measured at the earth also undergo short-term variations in intensity. Occasionally, the primary cosmic ray flux will suddenly decrease and then begin a slow recovery to normal levels again. This phenomenon, when correlated to a sudden increase in the plasma density and magnetic flux emitted from the sun (such as during a CME passage), is called a Forbush decrease. These short-term variations occur throughout the solar cycle, although they are more commonly observed during solar maximum. The magnitude of a Forbush decrease is variable, ranging from a few percent to as high as 35%, and depends on the strength of the magnetic disturbance propagating through interplanetary space (5). Two examples of Forbush decreases are shown in Figure 3 below. The first decrease occurred on 22 July, and is marked by a sudden decrease in the neutron monitor count rate by nearly 4%. The second decrease is much more significant, occurring early on 27 July, and marked by a decrease in the neutron monitor count rate by 10%. A characteristic rise in the count rate is seen soon after the decrease, and the count rates return to pre-disturbance levels after about 13 days.
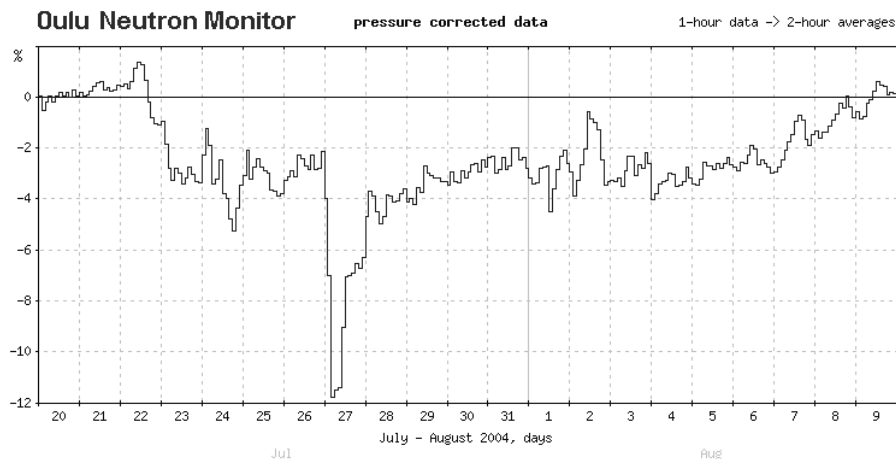
Figure 3: Two cosmic ray Forbush decreases observed at the Oulu neutron monitor in Finland over a period of three weeks during July and August of 2004. The first decrease occurred on 22 July; the second decrease occurred on 27 July. Count rates returned to normal levels by 8 August (2).

Solar Energetic Particles

Occasionally, the sun will eject a large amount of material, either through a solar flare or a CME. This material generally consists mostly of high-energy protons. If the mass of material is earth-directed, a significant increase in the flux of energetic particles may be observed. A solar proton event is defined as a sudden burst of high-energy particles from the sun, which can last up to several days. Operationally, the flux of particles with energies greater than 10 MeV must exceed 10 particles/cm^2/sec/str to qualify as a solar proton event; however, the types of solar proton events most threatening to human life occur less than once per decade. This makes them especially difficult to study or to predict (18).

Ground-based neutron monitors, which provide indirect measurements of the cosmic ray flux, occasionally detect short increases in cosmic ray intensities associated with increased solar activity (usually solar flares). After the initial increase, cosmic ray intensities return to normal levels within tens of minutes to days. Some of these increases in cosmic ray intensities are called ground level events (GLE). A GLE is defined as a sharp increase in the ground level neutron monitor count rate to at least 10% above the background, associated with solar protons of energies greater than 500 MeV (31). As of January 2006, only 69 GLEs have been observed since the first GLE was recorded in February of 1956 (3).

The GLE which occurred on 14 July 2000 is shown in Figure 4, as measured by the Oulu neutron monitor in Finland. A Forbush decrease is apparent on 13 July as the neutron monitor count rate drops sharply. The GLE is represented by the large spike in

the count rate on 14 July. A second Forbush decrease occurred on 15 July, coincident with the arrival of a fast-moving CME. A characteristic slow recovery in the count rate occurred over the next 15 days. The neutron monitor recorded the increased count rate from the GLE on the 14th despite the increase in magnetic activity which began a day prior.

Compared to galactic cosmic rays, solar energetic particles have relatively low energies, generally below 1 GeV, and only rarely are particles with energies greater than 10 GeV observed (11:37). The lower energies of solar energetic particles mean they are often not observed at low latitudes because of a phenomenon known as geomagnetic cutoff, which is discussed in Chapter II: Geomagnetic Cutoff.

Figure 4: Neutron monitor count rate from the Oulu neutron monitor in Finland. A GLE was recorded on 14 July 2000, indicated by the sharp spike in the neutron monitor count rate (11:129).

Just as in the case of galactic comic rays, the spectrum of solar protons can be reasonably represented by a power law in kinetic energy, E, (35)

$$F(E) = kE^{-\gamma} . \tag{3}$$

Even during a solar proton event, the cosmic ray spectrum above a few hundred MeV is composed almost entirely of galactic cosmic rays. However, solar energetic particles dominate the bulk of the cosmic ray spectrum below about 1 GeV during one of these events. This can be seen in Figure 5 below, which shows the relative importance of the galactic cosmic ray and solar energetic particle fluxes at different energies for a hypothetical solar proton event. At high energies (above a few GeV/nucleon) galactic cosmic rays are the dominant part of the spectrum. At low energies (below 1 GeV) solar energetic particles begin to dominate the overall spectrum (11).
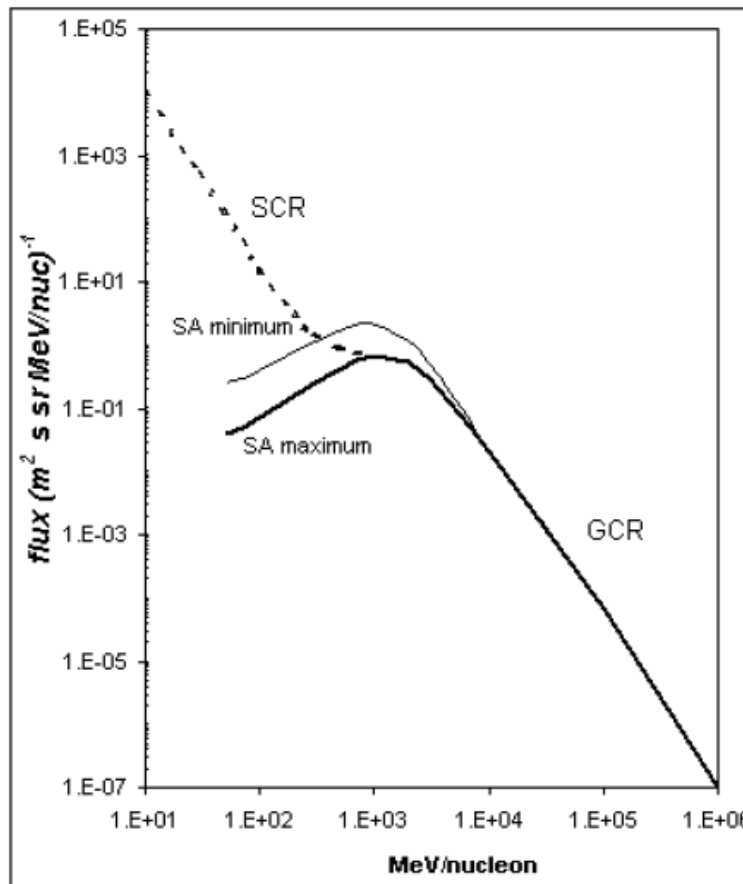
Figure 5: The galactic cosmic ray (GCR) and solar energetic particle, or solar cosmic ray (SCR) energy spectra. Solid lines are the galactic cosmic ray spectra for solar maximum and solar minimum. The dashed line shows the solar cosmic ray contribution to the overall spectrum (11).

18

An important question to ask is, "How big does a solar proton event need to be in order to significantly increase radiation levels at flight altitudes?" Or more appropriately (as will be shown later), "What does the spectrum of a solar proton event look like that increases radiation levels at flight altitudes?" The radiation exposure experienced by an aircrew will depend on both the size of the flux throughout the event, as well as the spectral hardness of the event (35). The flux can be measured directly by counting the number of particles that reach the earth's magnetic field. However, to compute the spectral hardness, the spectrum must be modeled using available information about the number of particles and their respective energies. An important concept in this discussion is rigidity.

Rigidity

Since both cosmic rays and solar energetic particles are charged particles, they are subject to the Lorentz force, and experience a $\overline{V} \times \overline{B}$ drift that continuously alters their trajectory. Energetic protons, whether solar or extra-solar in nature, must pass through the earth's magnetosphere in order to reach the atmosphere. A charged particle in a magnetic field will follow a spiral path with a radius of curvature r_b:

$$r_b = \frac{\gamma m_0 v_\perp}{Be},$$

(4)

where γ is the relativistic parameter, m_0 is the rest mass for the particle, $v_\perp = |v|\cos\theta$, or the velocity perpendicular to the magnetic field, B is the magnetic field strength, and e is the charge carried by the particle. The relativistic parameter γ is defined as

$$\gamma = \frac{1}{\sqrt{1 - v^2/c^2}}, \tag{5}$$

and the particle's perpendicular momentum is defined as

$$P_\perp = \gamma m_0 v_\perp. \tag{6}$$

Thus, the radius of curvature, also known as the gyroradius, is directly proportional to the momentum and inversely proportional to the magnetic field strength. However, the problem is made more complicated because the particle energies are typically high enough that the magnetic field changes significantly over one gyration. Therefore the simplification of assuming a uniform magnetic field cannot be made. Particles traveling along magnetic field lines are affected less because the perpendicular velocity is very small.

Given the dipole nature of the earth's magnetic field, charged particles approaching the earth in the ecliptic plane encounter magnetic field lines perpendicular to their trajectory. However, because particles traveling along magnetic field lines experience little to no deviation in their trajectories, the polar regions are the most accessible. To reach the equatorial regions, a proton cannot follow field lines, but must instead cross field-lines all the way down to the atmosphere. This is possible if the proton has sufficient energy (> 15 GeV), but so few particles have the requisite energy that the equatorial region is effectively forbidden to typical solar protons (26).

The magnetic rigidity, R, of a particle is a measure of its resistance to this effect. Rigidity (with units of momentum per unit charge) is a canonical variable and is

advantageous to use because all particles with the same value of R will follow the same path in a given magnetic field.

The radius of gyration in a given magnetic field depends on the momentum per unit charge (P/e), so it is convenient to discuss particle orbits in terms of rigidity:

$$R = \frac{Pc}{ze}, \tag{7}$$

where P is the momentum, c is the speed of light, z is the atomic number, and e is the electronic charge (positive for protons). The more energetic a particle is, the larger its gyroradius, and the higher its rigidity will be. Since $P \cdot c$ is typically expressed in electron volts and ze represents the number of electronic charge units, rigidity takes on units of volts (V). Convenient units are MV (10^6 V), and GV (10^9 V).

It is common to express energy in terms of rigidity and vice versa, therefore a conversion between the two units is necessary. The relativistic kinetic energy expressed in terms of kinetic energy per nucleon is

$$E_A = (\gamma - 1) E_{0A}, \tag{8}$$

where E_A is the kinetic energy per nucleon, and E_{0A} is the rest mass energy per nucleon. The rest mass energy of a proton is $m_0 c^2$, which is equal to 938.232 MeV. Conversion between kinetic energy per nucleon and rigidity is accomplished by using the following equation:

$$R = \frac{z}{A} (\gamma^2 - 1)^{\frac{1}{2}} E_{0A}, \tag{9}$$

21

where z is the atomic number and A is the atomic charge. The relativistic parameter γ can be computed from either the cosmic ray kinetic energy

$$\gamma = \frac{E_A + E_{0A}}{E_{0A}}, \tag{10}$$

or the cosmic ray rigidity (5)

$$\gamma = \left(\left(\frac{RA}{E_{0A}z}\right)^2 + 1\right)^{\frac{1}{2}}. \tag{11}$$

It is convenient to use equations in terms of rigidity. A table listing selected rigidity to energy conversions is contained in Appendix A for reference.

Geomagnetic Cutoff

The trajectory of a proton in the earth's geomagnetic field can be very complicated even if a simple dipole field is assumed (see Figure 8). The trajectory can be simplified by defining 'allowed' and 'forbidden' regions which may or may not be reached by a charged particle approaching the earth from infinity. To reach a certain magnetic latitude, λ_c, in a dipole magnetic field, the rigidity of the particle must exceed a certain cutoff rigidity, R_c. Particles of rigidity R_c reach latitudes greater than or equal to λ_c. Equivalently, at latitude λ_c only particles with rigidity equal to and greater than R_c would be expected to penetrate the magnetic field (9). For a given location on the Earth, the geomagnetic cutoff is the lowest rigidity that a particle can have and still traverse the magnetic field to be measured. All particles with lower rigidity will be deflected by the

magnetic field. Thus, geomagnetic cutoff rigidities provide a quantitative measurement of the shielding provided by the earth's magnetic field.

Geomagnetic field lines that extend out from the polar regions connect with the interplanetary magnetic field and present little or no barrier to incoming energetic particles. However, at lower latitudes the Earth's magnetic field acts as a filter that removes lower rigidity particles from the solar energetic particle or cosmic ray flux. The cutoff rigidity increases towards the geomagnetic equator.

Characterizing the earth's geomagnetic field can be difficult because it is affected by currents that exist within the magnetosphere. The distortion of the magnetic field because of these current systems causes a change in the geomagnetic cutoffs as well. Because magnetospheric currents have a significant effect on the cutoffs and because these external currents change significantly during a geomagnetic storm, it is necessary to calculate cutoffs globally for different levels of geomagnetic activity (15). Evidence of this dynamic cutoff phenomenon was observed during the large solar energetic particle event of 20 October 1989, where the cutoff latitude for a 100 MeV proton was observed to move 15 degrees equatorward during the geomagnetic disturbance (12).

Geomagnetic cutoffs are traditionally calculated by tracing test trajectories in a model magnetic field. Particle trajectories that are allowed to escape the Earth represent trajectories that would reach the earth from outside the magnetosphere, and are called allowed trajectories. Trajectories that do not escape the Earth, and instead are bent back around and impact the Earth, are called forbidden trajectories. The exact trajectory depends on the direction of arrival of the incoming particle in space and hence the cutoffs

23

are a function of direction at a specified point near the Earth. The usual method for determining cutoffs is to compute trajectories of particles from a given point near the earth at successively lower energies until the forbidden trajectories are found.

Unfortunately, trajectories often exhibit chaotic behavior, especially near the cutoff, and hence the cutoffs are not always sharp. Instead, they typically consist of bands of allowed and forbidden regions. The upper cutoff rigidity R_U is the highest detected allowed/forbidden transition – all particles above this rigidity are allowed. The lower cutoff rigidity R_L is the lowest allowed/forbidden transition – all particles below this rigidity are forbidden. The region in between is called the cosmic ray penumbra and is characterized by a complicated number of allowed and forbidden trajectories. No simple method of organizing the trajectories within the penumbra exists as of yet (5:6-9). Attempts have been made to come up with a number called the effective cutoff rigidity R_C to characterize this region. The effective cutoff rigidity is a linear average of the allowed bands within the penumbra that attempts to account for the transparency of the penumbra (29:96). Figure 6 shows the geomagnetic cutoffs and the structure of the penumbra for three locations in North America. The white bands are allowed trajectories; the black bands are forbidden trajectories. In the example below, the lower cutoff at Newark is 1.90 GV, while the upper cutoff is 2.30 GV. The penumbra is located between these two values, and the chaotic behavior of the cutoff inside the penumbra is evident. Note also that the penumbra varies in size and complexity between locations.

An illustration of the width of the cosmic ray cutoff penumbra as a function of latitude and rigidity is shown in Figure 7. The upper, lower, and effective cutoffs were

computed assuming a vertically incident particle. The width of the penumbra is illustrated by the shaded region of the plot. The solid line denotes the effective cutoff rigidity. This shows the complexity of the penumbral region and the computed effective cutoff rigidity. The penumbra increases in size as rigidity increases or latitude decreases. Poleward of 60 degrees latitude, the penumbra nearly vanishes (see Figure 20).
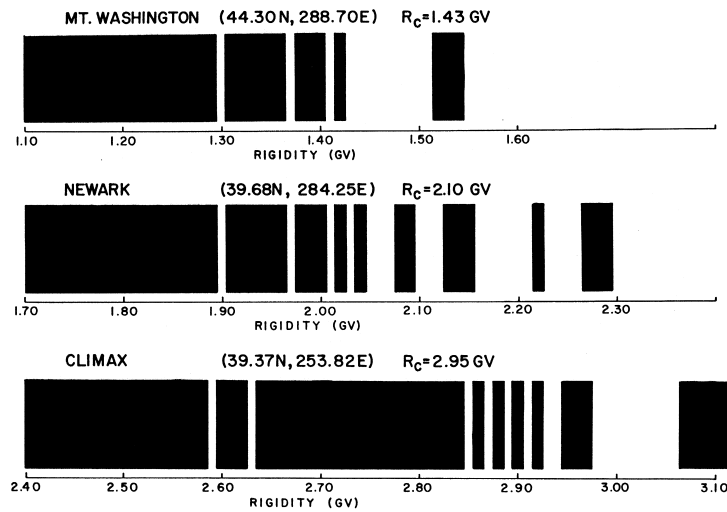
Figure 6: Cosmic ray cutoffs and the cosmic ray penumbra for vertically incident charged particles. White bands depict allowed rigidities, black bands depict forbidden rigidities. The penumbra extends from the white band at the lowest rigidity to the black band at the highest rigidity (27).

The main reason why it is so difficult to quantify the cutoff rigidity is because the equations of charged particle motion within a magnetic field do not have any solution in closed form (28:6-10). As a result, the global calculation of geomagnetic cutoff rigidities is computationally intensive and if performed in the traditional way, may not meet time constraints associated with real-time operations. This challenge can be met by using a number of approximations and by using specialized cutoff search strategies. These techniques will be discussed later in Chapter III.
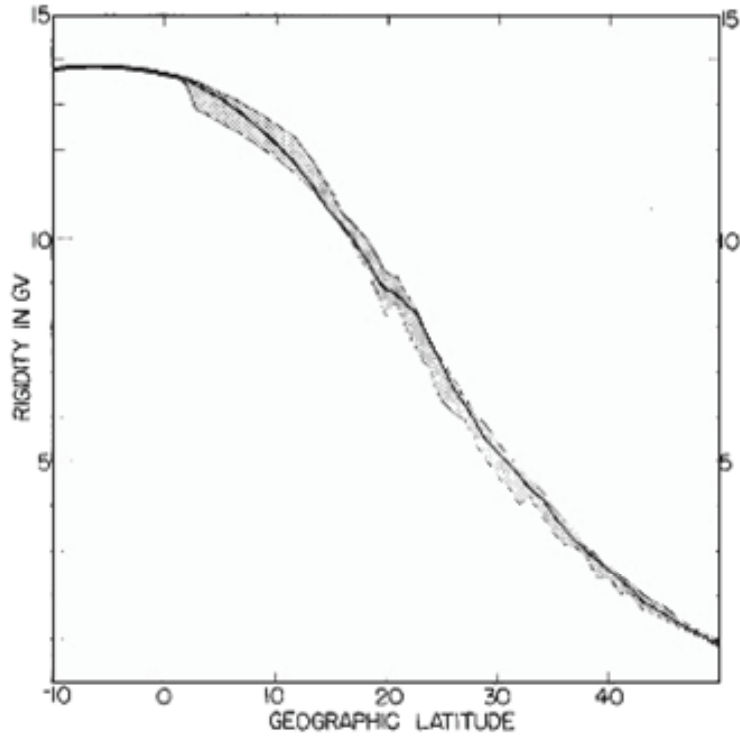
Figure 7: Illustration of the width (shaded area) of the cosmic ray vertical cutoff penumbra as a function of latitude along the 260°E meridian. The solid line indicates the effective geomagnetic cutoff rigidity along this meridian (26:6-9).

Particle Access to the Atmosphere

Early cosmic ray measurements showed that the cosmic ray intensity was ordered by magnetic latitude. Störmer developed the early theory of particle trajectories in the magnetosphere. Unfortunately, as mentioned earlier, the resulting equations to describe these motions are complicated and have no closed form solution (16).

A special case solution exists in a dipole magnetic field which describes the geomagnetic cutoff rigidity. If the earth's magnetic field is approximated as a dipole magnetic field, the geomagnetic cutoff rigidity can be calculated using the following equation:

26

$$R_c = \frac{M \cos^4 \lambda}{r^2 \left(1 + \left(1 - \sin \varepsilon \sin \phi \cos^3 \lambda\right)^{\frac{1}{2}}\right)^2} \,, \qquad (12)$$

where R_c is the geomagnetic cutoff rigidity in MV, M is the earth's dipole moment, λ is the geomagnetic latitude, ε is the zenith angle (where the zenith direction is a radial from the position of the dipole center), and ϕ is the azimuth angle measured from magnetic north (28:6-11). This equation can be simplified by normalizing to the earth's dipole moment M and expressing the distance from the dipole center r in earth radii, such that the constant terms evaluate to 59.6 (28:6-12). Further, if a vertical (radial direction) cutoff is assumed, the zenith angle goes to zero and Eq. (12) reduces to the following equation for the vertical cutoff rigidity (28:6-12):

$$R_{cv} = \frac{14.9 \cos^4 \lambda}{r^2} \,. \qquad (13)$$

This greatly simplifies the process for estimating cutoff rigidities. The two assumptions made are that incoming charged particles are vertically incident and that the earth's magnetic field can be approximated with a dipole magnetic field.

In Figure 8 below, some numerical trajectory calculations made for protons of different rigidities are illustrated. All of the trajectories in this figure were initiated in the vertical direction from the same location. Rigidities decrease for each successive trajectory, beginning with the trajectory labeled 1. The trajectories labeled 1, 2, and 3 show increasing geomagnetic bending before escaping into space. The trajectory labeled 4 develops intermediate loops before escaping. The lower rigidity trajectory labeled 5 develops complex loops near the earth before it escapes. As the charged particle rigidity

is further reduced, there are a series of trajectories that intersect the earth (i.e. re-entrant trajectories). In a pure dipole field that does not have a physical barrier embedded in the field, these trajectories may be allowed, illustrating one of the differences between Störmer theory and trajectory calculations in the earth's magnetic field. Finally, the still lower rigidity trajectory labeled 15 escapes after a series of complex loops near the earth. These series of allowed and forbidden bands of particle access are the cosmic ray penumbra. They also illustrate an often-ignored fact that cosmic ray geomagnetic cutoffs are not sharp (except for special cases in the equatorial regions) (27).
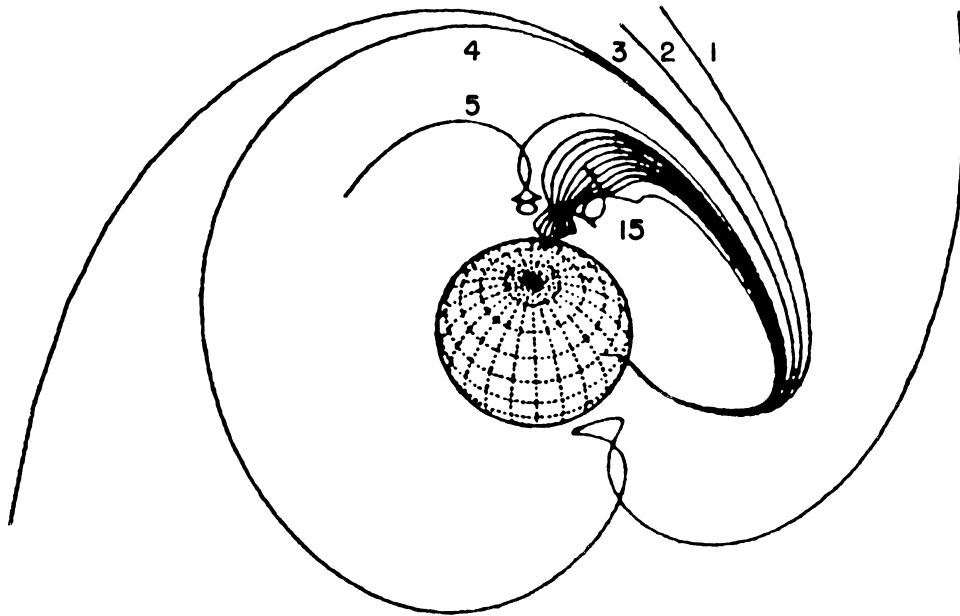
Figure 8: Illustration of proton trajectories of different rigidities in the geomagnetic field. The paths are very complicated even if a simple dipole field is assumed. Trajectories near the cutoff rigidity exhibit complex behavior. The rigidity of trajectory 1 is the greatest, with rigidities decreasing for each subsequent trajectory shown (27:5).

A plot of the Störmer cutoff latitude against energy for both protons and electrons is shown in Figure 9. Based on the figure, it is evident that protons require energies

greater than 1 GeV to reach a dipole latitude of 50 degrees; electrons require even more

energy to reach the same latitude. This is because the mass of an electron is much

smaller compared to the mass of a proton, and the gyroradius is proportional to the mass,

as in Eq. (4). Equivalently, the rigidity of an electron is much smaller than that of a

proton.
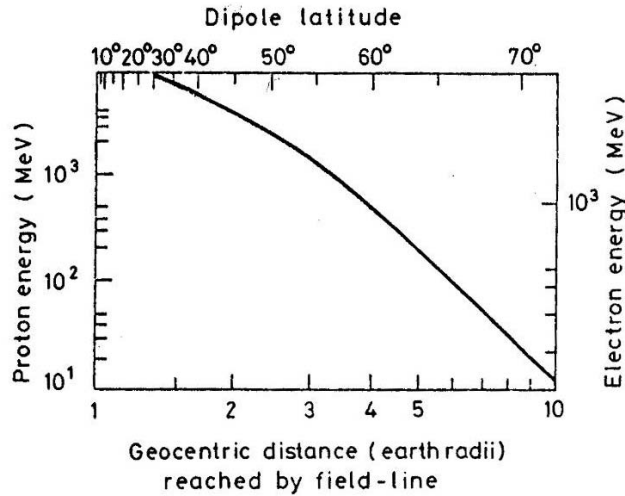
Figure 9: Plot of the Störmer cut-off latitude vs. energy (log scale) for protons and electrons. A particle's cutoff latitude decreases as its energy increases. Electrons require greater energies than protons to reach the same latitude because electrons have much smaller gyroradii (9:357).

The Störmer values are not without errors since they assume a dipole magnetic

field with no disturbances. The quiet magnetic field is not strictly dipolar, and currents

within the magnetosphere along with distortions of the geomagnetic field by the solar

wind can both reduce the cutoff latitude. Figure 10 shows the difference in cutoff latitude

between the dipole field and a more realistic field. The cutoff latitude may be reduced

further if a magnetic storm, which enhances the ring current and moves the magnetopause

inward, occurs at the same time. The induced current in the magnetosphere affects the

geomagnetic field in a complex manner, changing the distribution of the cutoff rigidities

and usually reducing them (15).
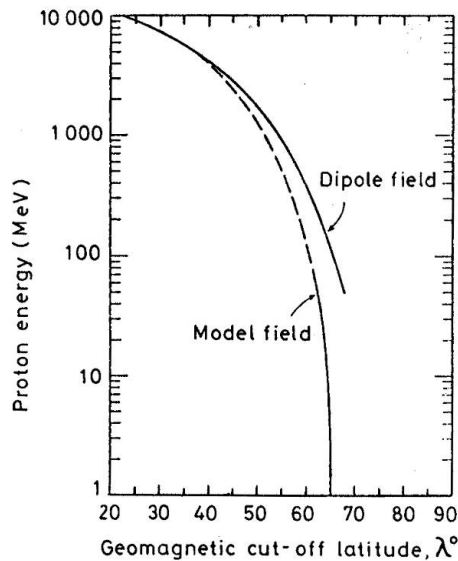
Figure 10: Differences between a dipole magnetic field and a more realistic geomagnetic field. Geomagnetic cutoff latitudes are reduced for the more realistic magnetic field at energies less than 4 GeV. The model field takes into account distortions caused by the solar wind (9:358).

Production of Secondary Particles

When an energetic proton crosses the earth's magnetic field and enters the

atmosphere, it loses energy in collisions with the neutral molecules and leaves an ionized

trail. Substantial ionization can occur down to 50 km in some cases. Solar protons

therefore ionize a region below the normal ionosphere, and can enhance radiation levels

at altitudes where aircraft commonly operate.

The mean free path of energetic protons in the atmosphere is approximately

100 g/cm^2 (11:133). This is determined mainly by collisions between protons and the

nuclei of atmospheric atoms. However, an incident proton will have to traverse

approximately 1033 g/cm² of atmosphere to reach the earth's surface. But after

traversing only 58 g/cm² of air mass, the primary proton flux is reduced to about half of

the initial flux. Thus it is unlikely that a substantial number of energetic protons will

penetrate to the earth's surface without undergoing a number of collisions.

The successive collisions between the incident particles and the atmospheric

nuclei, and their respective interactions are called an atmospheric cascade. The cascade

consists of three main components: the "soft" or electromagnetic component, which is

made up of electrons, positrons, and photons; the "hard" or muon component, made up of

muons; and the nucleonic component, which consists mostly of suprathermal neutrons

(11). A typical atmospheric cascade is depicted below in Figure 11.
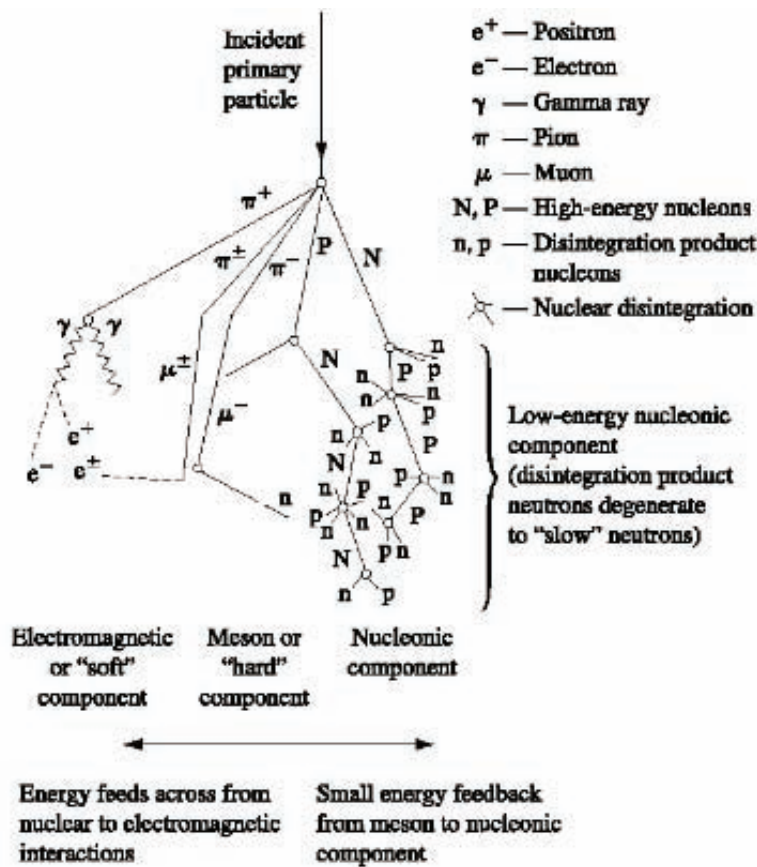
Figure 11: Schematic diagram of an atmospheric cascade (29:135).

The collisions between primary cosmic rays and air nuclei produce high-energy secondary cosmic rays as well as neutrons. We are able to measure the flux of neutrons produced by these cosmic ray showers at the surface of the earth using neutron detectors. As the protons penetrate deeper into the atmosphere, the atmospheric density increases, causing the frequency of collisions and the number of secondary particles produced to increase. The number of secondary particles produced becomes significant at about 55 km, with the maximum in their intensity occurring at approximately 20 km. The intensity of the secondaries then decreases to the surface of the earth as particles lose energy through additional collisions until the majority either decay or are absorbed (5).

Particle Transport and Monte Carlo Simulations

The intensity and composition of the cosmic rays observed within the atmosphere depend on the quantity of the absorbing material traversed before observation, in addition to the cutoff rigidity of the observation point. Atmospheric conditions, especially barometric pressure, also have an appreciable effect on the measured intensity. Thus cosmic ray intensities are usually reported in terms of atmospheric depth (mass of air per unit area above the observation point) or of barometric pressure at the observation point rather than the altitude of observation. The ionization rate measured within the atmosphere depends on the amount of matter above the point of observation and on its distribution with height. The altitude or atmospheric depth at which the energetic particles are measured makes a significant difference in the shape and energy range of the spectrum. Once the protons begin to encounter the atmosphere, fewer and fewer of the

primary proton flux will be available for measurement. Thus it is best to measure the proton flux before it encounters the atmosphere.

In the past, theoretical predictions of atmospheric particle fluences have been subject to large uncertainties. The primary spectrum was known only within a factor of two and the demand in computing power for three-dimensional Monte Carlo simulations made systematic studies of all aspects of the radiation field almost impossible. Most studies were based on two-dimensional calculations which cannot predict isotropically distributed quantities. Recently however, the situation has greatly improved as detailed experimental information on the primary cosmic ray spectra is now available and powerful CPUs have become relatively inexpensive. In addition, results of systematic experimental studies performed aboard aircraft, balloons, and on the ground exist with which the model predictions can be compared.

The work used in this study was performed using Monte Carlo simulations. Specifically, a Monte Carlo code called MCNPX 2.4.0 was used. MCNPX, which stands for Monte Carlo N-Particle eXtended, is a general-purpose Monte Carlo radiation transport code for modeling the interaction of radiation. Results from these simulations were used to generate fluence to effective dose rate conversion factors which will be discussed later in Chapter III: Effective Dose Calculation.

Measurement of Solar Energetic Particles

Only a few satellites carry equipment designed to measure the flux of energetic particles in the near-earth environment. For the calculations in this paper, the data presented is from the National Oceanic and Atmospheric Administration's (NOAA)

Geostationary Operational Environmental Satellites (GOES), unless otherwise noted. NOAA has several GOES spacecraft in operation. From 1995 through 2003, the primary sensor for measuring energetic particles was on the GOES-8 spacecraft, and from 2003 through 2005, the main sensor was on the GOES-11 spacecraft. GOES-10 was used as the primary sensor briefly in April-May 2003, however intermittent sensor problems prevented it from remaining as the primary sensor. A sensor is also present on the GOES-12 spacecraft (33).

Prior to GOES-8, the GOES series spacecraft were spin-stabilized. Particle detectors used on these satellites were thus omni-directional because they were able to observe particles coming from almost any direction. However, GOES-8 and subsequent satellites are three-axis stabilized which means the energetic particle sensor looks only in one direction. It has been shown however that this does not significantly compromise the detector's ability to recognize event onsets, and further that the fluxes of particles observed by GOES spacecraft at different longitudes differed by less than 20% at relativistic energies, and the differences decreased with decreasing energy (24:10). Further, no significant evidence of anisotropy effects was found between the different locations of the sensors. Therefore, dose rate estimates calculated using the procedure outlined in Chapter III can be expected to contain uncertainties of approximately 10% between the different operational GOES spacecraft (24:10).

The NOAA Space Environment Center (SEC) monitors the near-earth space environment using a set of instruments onboard the GOES spacecraft called the Space Environment Monitor (SEM). The instruments used for the purposes of this paper are the

Energetic Particle Sensor (EPS), which measures low energy protons from 0.8 to 500 MeV, and the High Energy Proton and Alpha Detector (HEPAD), which measures protons with energies above 330 MeV and alpha particles with energies above 640 MeV/nucleon (34).

The EPS measurement of protons is divided into seven differential channels, labeled P1 – P7. Channels P1 – P3 are obtained from small angle solid-state telescopes, while channels P4 – P7 are obtained from several large aperture dome detectors. The HEPAD measurement of protons is divided into 4 channels, labeled P8 – P11. These channels are obtained from a solid-state/Cerenkov telescope (24). The characteristics and individual responses for each channel will be discussed later in Chapter III: Correction Factors for GOES Energetic Particle Measurements. GOES energetic particle data can be obtained from the NOAA National Geophysical Data Center (NGDC) (13).

The CARI-6 Radiation Dose Predictive Code

CARI-6 is a computer code designed to calculate the cumulative radiation dose received during a flight. The latest version incorporates the 1995 International Geomagnetic Reference Field (IGRF) as well as a re-analysis of the primary cosmic ray spectrum. The program is based on a computer code called LUIN, which is a high-energy transport code based on the solution to the Boltzmann equation (16).

Although the code does take into account some form of geomagnetic cutoff rigidity and a measure of the solar output, the values are calculated using a monthly mean heliocentric potential, and thus do not accurately account for large, short-lived solar disturbances, such as solar flares or CMEs. The CARI-6 code will generally over-predict

dose rates during Forbush decreases when the cosmic ray flux is suppressed because of magnetic activity. The code also does not account for large changes in geomagnetic cutoff rigidity during geomagnetically active times. Outside of these events, the CARI-6 code provides excellent agreement between theory and measurement (16). However, there is still a need for a method to compute dose rates due to solar energetic particles, for those rare events when solar activity greatly enhances radiation dose rates.

III. Methodology

Chapter Overview

This chapter covers the methods by which the spectrum of incoming solar energetic particles will be modeled as well as the way in which dose rates at given altitudes and locations will be computed. First, energetic proton measurements are obtained from GOES-11 spacecraft orbiting the Earth. Next, the spectrum of the incoming solar proton flux is modeled using a power law in rigidity. Then, making use of transport codes and radiation exposure coefficients, effective dose rates are calculated. Geomagnetic cutoff effects will be introduced and applied to the dose rate calculation. Lastly, assumptions and known sources of error will be discussed.

The method for determining effective dose rates outlined below was developed by *Copeland et al*. (1). Any deviations from their original methods will be noted.

Correction Factors for GOES Energetic Particle Measurements

In calculating the dose rate due to solar energetic particles, the energy spectrum of the incoming particles must first be modeled. This requires specific information about the flux and energy of particles incident in the earth's upper atmosphere, which is available from the GOES Space Environment Monitor. Unfortunately, the measurements are not reported as raw count rates. Instead, several correction factors are automatically applied to convert the satellite count rates to fluxes. However, these numbers are calibrated for the older GOES instruments (GOES-7 and previous). The newer satellites (GOES-8 and later), require different correction factors.

The GOES Space Environment Monitor discussed previously in Chapter II records the flux of energetic particles in 11 different channels. The first seven channels are used by the EPS instrument and the remaining four channels are used by the HEPAD instrument. Table 2 below shows the energy ranges for each of these channels.

Table 2: Rigidity (energy) ranges for GOES Space Environment Monitor instruments. For the calculations in this study, channels P4 – P7 and P10 – P11 are used (24:3).

Channel	Rigidity (Energy) Range Units – MV (MeV)
P1	36.3 – 88.9 (.7 – 4.2)
P2	88.9 – 128.1 (4.2 – 8.7)
P3	128.1 – 165.6 (8.7 – 14.5)
P4	168.5 – 276.9 (15 – 40)
P5	269.8 – 400.8 (38 – 82)
P6	405.9 – 644.6 (84 – 200)
P7	467.6 – 1581.0 (110 – 900)
P8	853.5 – 982.3 (330 – 420)
P9	982.3 – 1103.4 (420 – 510)
P10	1103.4 – 1343.2 (510 – 700)
P11	> 1343.2 (> 700)

Each channel is sensitive to a range of energies and has a characteristic energy which will be used to derive a flux spectrum for the particles measured. For the purposes of this study, channels P4 – P7 will be used to cover rigidities of 137 to 1225 MV (10 to 604 MeV), and channels P10 – P11 will be used to cover rigidities 1225 to 32545 MV (604 to 31620 MeV). Channels P4 – P10 are in terms of differential flux, with units of protons/cm^2/sec/str/MeV. However, channel P11 is in terms of integral flux, with units of protons/cm^2/sec/str. The data from these channels can be used to construct a piecewise-continuous approximation of the true solar proton spectrum.

In their procedure for modeling the spectrum of incoming solar energetic particles, *Copeland et al.* (1) use the numbers in Table 3 to correct the data from the GOES Space Environment Monitor (1:2). These correction factors may be applied to data from GOES-8 and newer spacecraft (24:6).

Table 3: Conversion factors and characteristic rigidities for use with GOES-8 and newer spacecraft (1).

Channel	Conversion Factor (k)[a]	Conversion Factor (k')[b]	Characteristic Rigidity (MV)
P4	4.64	22.25	225.1
P5	15.5	43.04	338.2
P6	90.	252.8	563.9
P7	300.	1210.	950.
P10	162.	175.6	1225.
P11	1565.	1103.	1700.

[a] k : counts/(particles/cm^2/str/MeV)
[b] k' : counts/(particles/cm^2/str/MV)

The first step in modeling the spectrum of incoming protons is to apply several correction factors to the data from the GOES instruments to convert the incorrect fluxes to raw count rates and then to the correct fluxes. The correction factors are listed by *Panametrics* (24). To convert the incorrect fluxes back to the raw instrument count rates, the flux in each channel must be multiplied by the appropriate conversion factor listed in Table 3. Next, the background galactic cosmic ray count rate must be subtracted from the total count rate since only the solar proton count rate is of interest. This is accomplished by averaging the count rate over the previous 12 hours of quiet-time measurements (outside of any significant solar activity) in each channel and subtracting

from the total count rate in each channel (1:1). This ensures the spectrum being modeled is that of solar protons alone, with no contribution from galactic cosmic rays.

The instrument count rate due to solar protons must be converted to a differential flux. This is accomplished by dividing the count rate in each channel by the appropriate conversion factor (k') listed in Table 3. This returns a differential flux $f(R)$ with units of particles/cm^2/str/MV. With the differential flux in each rigidity channel, a preliminary spectral hardness index can be calculated. The spectral hardness of the incoming protons is a measure of how much energy the particles have, and is a key factor in modeling the spectrum. The higher the flux of high-energy particles, the harder the spectrum will be.

Characterization of the Energy Spectrum / Spectral Hardness

With the correct differential fluxes in each of the channels, a spectral hardness, γ, and intensity, α, can be calculated for each channel which allows an approximation of the entire energy spectrum to be constructed. Recall from Chapter II that the energy spectrum of solar protons can be represented by a power law of the form:

$$f(R) = \alpha R^{-\gamma}. \tag{14}$$

To fit the solar proton flux to a power law, the intensity, α, and the spectral hardness index, γ, must be determined.

A preliminary spectral hardness index ($\gamma_{Pi,Pj}$) is computed between adjacent channels. Thus the computation of $\gamma_{P4,P5}$ uses channels P4 and P5. To calculate the preliminary spectral hardness, the following equation is used:

$$\gamma_{Pi,Pj} = \frac{\ln\left[f\left(R\right)_{Pi}\right] - \ln\left[f\left(R\right)_{Pj}\right]}{\ln\left[R_{Pj}\right] - \ln\left[R_{Pi}\right]} \, , \tag{15}$$

where $f\left(R\right)_{P4}$ through $f\left(R\right)_{P11}$ are the differential proton fluxes derived in the previous

section, and R_{P4} through R_{P11} are the characteristic rigidities for each channel listed in

Table 3 (1).

This preliminary spectral hardness is used to correct the differential flux of solar

particles according to the processing procedure for the EPS and HEPAD sensors (24:13,

15). This process is outlined in greater detail by *Copeland et al.* (1:3). In performing this

correction, the spectral response is being weighted towards the higher energies. For

further information about this correction, see the technical document concerning data

processing and the analysis of GOES particle data prepared by *Sauer* (24:11).

Once the differential flux has been corrected, the spectral hardness ($\gamma_{Pi,Pj}$) must

be recalculated using Eq. (15) and the corrected fluxes. With the spectral hardness

computed, the intensity α can be computed for each channel using

$$\alpha = \frac{f\left(R\right)_{corrected}}{R^{-\gamma}} \, , \tag{16}$$

where $f\left(R\right)_{corrected}$ is the corrected differential flux, and R is the characteristic rigidity

for the respective channel listed in Table 3 (1).

Channel P11 needs further manipulation before a piecewise-continuous

description of the spectrum can be constructed. This channel is unique in that it

represents an integral flux. The process has proceeded up until now treating channel P11

in the same way as the other channels in order to assist with the computation of spectral

hardness values. However, the channel P11 count rate must be converted to a corrected

integral flux. To do this, the count rate must be divided by 0.73 cm^2·str, which is the

geometric factor listed by the instrument's manufacturer for channel P11 (24:6).

To compute the spectral hardness for channel P11, Eq. (17) is used to find the

value of γ that best describes the corrected integral flux (F_{P11}) derived for channel P11.

To do this, γ is set equal to $\gamma_{P10,P11}$ and subsequently decreased in steps of 0.000001 until

the following equation is satisfied (1:3):

$$F_{P11} \leq \int_{1343MV}^{32545MV} \alpha R^{-\gamma} dR \,. \tag{17}$$

Here, F_{P11} is the corrected integral flux for channel P11, α is the intensity and is set to

the same value as computed for channel P10; R is the characteristic rigidity for channel

P11 listed in Table 3.

In the case that F_{P11} is greater than the integral in Eq. (17), the following equation

is used:

$$F_{P11} \leq \int_{1343MV}^{1344MV} \alpha R^{-\gamma} dR \,, \tag{18}$$

and the upper limit of integration is increased in steps of 1 MV until the inequality is

satisfied (1:3).

Once values for intensity, α, and spectral hardness, γ, have been calculated for

each rigidity channel, they are used in conjunction with Eq. (3) to create a piece-wise

spectrum spanning the full range of rigidities. Together, the reconstruction describes the solar proton spectrum from 137 to 32,545 MV (10 to 31,620 MeV) (1:3).

This procedure was carried out for the solar proton event and associated ground level event (GLE) of 20 January 2005 to produce Figure 12 below. The spectrum was modeled at three times – 0655 UT, 10 minutes later (0705 UT), and 2 hours later (0855 UT). Since the process removes the background galactic cosmic ray flux prior to modeling the spectrum, the spectra shown below describe only the solar proton flux.
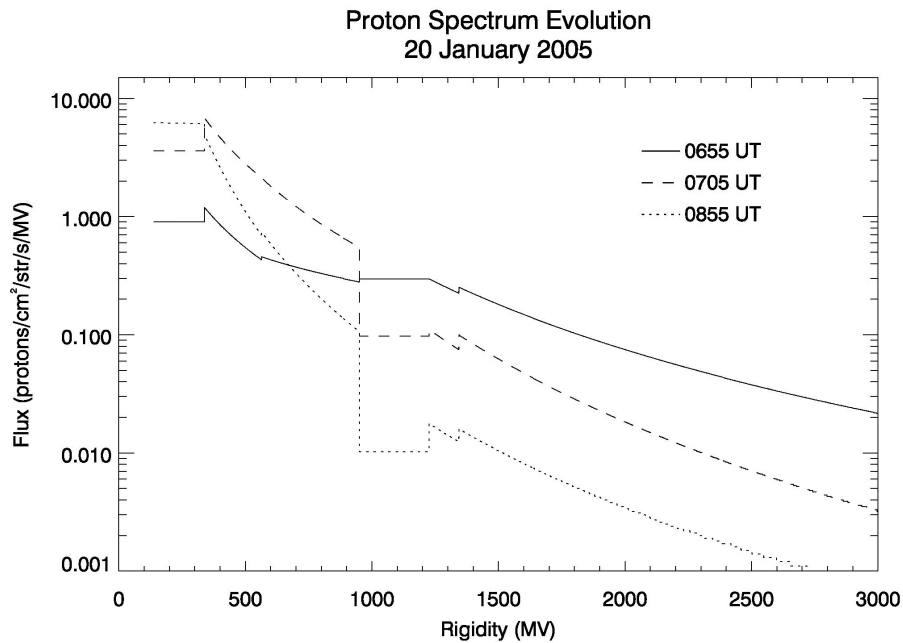
Figure 12: Evolution of the solar proton spectrum for the 20 January 2005 solar proton event and associated GLE. The background galactic cosmic ray flux has been removed. Peak dose rates associated with this event occurred at 0655 UT.

At 0655 UT, the spectrum was extremely hard, indicating a large flux of high energy protons. In fact, solar protons with rigidities of nearly 22 GV (21 GeV) were measured. This event was rare in that it produced the largest GLE observed in 50 years.

After 0655 UT, the spectrum softened, with fluxes of lower energy particles increasing and fluxes of higher energy particles decreasing. The discontinuous nature of the plot is an unavoidable byproduct of the method used to model the spectrum. More discussion on this problem will follow in Chapter IV.

Once the rigidity spectrum of the solar proton flux has been modeled, it can be used it to calculate the effective dose rate expected at a specified altitude.

Effective Dose Calculation

To calculate the effective dose rate at a specific altitude, the method for modeling the solar proton spectrum developed by *Copeland et al.* (1) and described in the previous section is used, along with the data contained in Table 4 below. This table was generated using the multipurpose particle transport code MCNPX 2.4.0, and shows the effective dose rate per unit flux of primary solar protons, as related to incident rigidity and energy at selected altitudes above mean sea level. To run the MCNPX 2.4.0 code and generate the effective dose rate per unit flux, the earth, its atmosphere, and the near-earth environment had to be modeled and input into the simulation (1:2). The MCNPX simulations were performed by *Copeland et al.* (1:2).

The secondary particle flux was generated by the MCNPX code by assuming an incident proton flux at the top of the atmosphere, which was assumed to be at an altitude of 100 km. Further, since the GOES energetic particle data does not contain any directional information (because the satellites are three-axis stabilized), the proton flux was assumed to be isotropic. This may not be a good assumption during the early stages of a solar proton event, where it has been shown that the solar energetic particle flux from

44

solar activity in the sun's western hemisphere is usually anisotropic (30:109). However, any anisotropies in the solar particle flux are eventually eliminated by the spreading effect of the interplanetary and earth's magnetic fields. Depending on the initial anisotropy of the event, and the strength of the magnetic field, this process may take a few minutes to a few hours (7:2).

The GOES Space Environment Monitor is located at an altitude of approximately 35,000 km in geosynchronous orbit. Obviously, this is farther away than 100 km from the ground where we are assuming the particles begin to interact with the atmosphere. The atmospheric pressure density at 100 km is approximately 0.0003 g/cm^2 (12), and accounting for the remaining atmosphere above this altitude would not significantly improve the dose estimates (1:2).

The earth was modeled in the MCNPX code as a sphere of liquid water with a radius of 6371 km and a density of 1 g/cm^2. The Earth's atmosphere was modeled as a series of 100 spherically symmetric layers, each 1 km thick, consisting of a gaseous mixture of nitrogen, oxygen, argon, and carbon atoms. The density of each layer was input as the density reported for the middle of the layer using the U.S. Standard Atmosphere from 1976 (12). The result was an atmosphere with a vertical depth of 1035.08 g/cm^2 (1:2).

Fluence-to-effective-dose conversion coefficients derived by *Pellicioni* (17:A1.7) were used to convert the secondary particle fluences generated by the MCNPX 2.4.0 code into effective dose rates per unit flux, with units of $\mu Sv/hr/(protons/cm^2/sec/str)$. The

results are listed in Table 4 below, and can be used for any solar particle event, however, geomagnetic cutoff effects have not been taken into account (1:2).

To calculate the effective dose rate ($E(H)$ with units of μSv/hr) for a specific altitude, the following equation is used:

$$E(H) = \int_{R_{min}}^{R_{max}} \psi(R) \Delta(R,H) dR, \tag{19}$$

where $\psi(R)$ is the solar proton spectrum approximated using the algorithm described in the previous section, $\Delta(R,H)$ is the effective dose rate per unit flux (from Table 4), R_{min} is the lower rigidity limit of channel P4, and R_{max} is the upper rigidity limit found using either Eq. (17) or Eq. (18) (1:3). Integrating Eq. (19) over 1 MV-wide steps from R_{min} to R_{max} gives the total dose rate for a specific altitude.

The methods outlined above were used to create Figure 13 below. The plot shows the effective dose rate for 20 January 2005 at three selected altitudes. The event onset was 415 minutes after 00 UT (0655 UT). After the peak, the dose rates decreased as the spectrum softened. For a hypothetical 3-hour flight at 80,000 feet beginning at 0655 UT, the total dose accrued would be 110.10 μSv, or 0.11 mSv. A longer 10-hour flight at this altitude would cause a slightly larger total dose of 155.61 μSv. These values do not take into account geomagnetic cutoff or any contribution from the galactic cosmic ray flux.

Table 4: Effective dose rate per unit flux of primary solar protons at selected altitudes (H) above mean sea level. Note that geomagnetic cutoff effects have not been taken into account as of yet (1).

Dose rate per unit flux, $\Delta(R,H)$. Units are μSv/hr/(protons/cm^2/sec/str)				
Rigidity (R), MV	Energy, MeV	H=-50ft	H=9722ft	H=19,588ft	H=29,378ft
183.5	17.78	1.000×10^{-12}	1.000×10^{-12}	1.000×10^{-12}	2.901×10^{-9}
245.6	31.62	1.000×10^{-12}	1.000×10^{-12}	1.404×10^{-10}	1.256×10^{-8}
329.7	56.23	1.000×10^{-12}	1.000×10^{-12}	2.978×10^{-9}	2.063×10^{-7}
444.6	100	1.000×10^{-12}	9.739×10^{-9}	2.251×10^{-7}	7.796×10^{-6}
604.4	177.8	9.040×10^{-8}	1.919×10^{-7}	7.713×10^{-6}	1.271×10^{-4}
832.7	316.2	5.281×10^{-7}	2.489×10^{-5}	2.935×10^{-4}	1.960×10^{-3}
1171	562.3	7.556×10^{-6}	2.383×10^{-4}	2.267×10^{-3}	1.207×10^{-2}
1696	1000	4.294×10^{-5}	1.122×10^{-3}	9.903×10^{-3}	5.130×10^{-2}
2549	1778	2.173×10^{-4}	4.428×10^{-3}	3.625×10^{-2}	0.1469
3991	3162	7.719×10^{-4}	1.495×10^{-2}	9.106×10^{-2}	0.3009
4848	4000	1.122×10^{-3}	1.915×10^{-2}	0.1147	0.3651
6495	5623	1.885×10^{-3}	2.356×10^{-2}	0.1319	0.4335
10898	10000	7.433×10^{-3}	4.966×10^{-2}	0.2413	0.7315
18695	17780	2.202×10^{-2}	0.1064	0.4464	1.277
20917	20000	2.751×10^{-2}	0.1227	0.5025	1.41
32545	31620	6.046×10^{-2}	0.2178	0.7942	2.11
		H=39,197ft	H=48,977ft	H=58,749ft	H=68,511ft	H=78,260ft
183.5		8.348×10^{-8}	1.282×10^{-6}	7.556×10^{-6}	1.937×10^{-5}	3.215×10^{-5}
245.6		9.257×10^{-7}	1.521×10^{-5}	7.390×10^{-5}	1.699×10^{-4}	2.622×10^{-4}
329.7		1.199×10^{-5}	1.223×10^{-4}	4.873×10^{-4}	1.004×10^{-3}	1.456×10^{-3}
444.6		1.511×10^{-4}	7.832×10^{-4}	2.407×10^{-3}	4.436×10^{-3}	6.602×10^{-3}
604.4		1.046×10^{-3}	4.495×10^{-3}	1.129×10^{-2}	1.165×10^{-2}	2.446×10^{-2}
832.7		8.491×10^{-3}	2.470×10^{-2}	5.079×10^{-2}	0.1116	0.2307
1171		4.331×10^{-2}	0.1298	0.2748	0.385	0.449
1696		0.1731	0.3447	0.4922	0.5712	0.59
2549		0.3629	0.5957	0.7517	0.7941	0.7719
3991		0.6252	0.9125	1.064	1.077	1.004
4848		0.7475	1.079	1.243	1.242	1.15
6495		0.9214	1.379	1.621	1.653	1.518
10898		1.484	2.1	2.357	2.296	2.075
18695		2.418	3.234	3.451	3.241	2.835
20917		2.638	3.499	3.711	3.45	3.006
32545		3.792	4.795	4.884	4.425	3.762

This event was unique in that it produced the largest ground level event (GLE) observed in over 50 years. Events which produce such high dose rates are very rare. However, even with an extremely rare event such as this one, it is obvious that the bulk of the accrued dose rate occurs during the few minutes to hours immediately following the event onset. This is the time period most critical to avoid. This event will be compared with other recent significant events in Chapter IV: Event Comparisons.
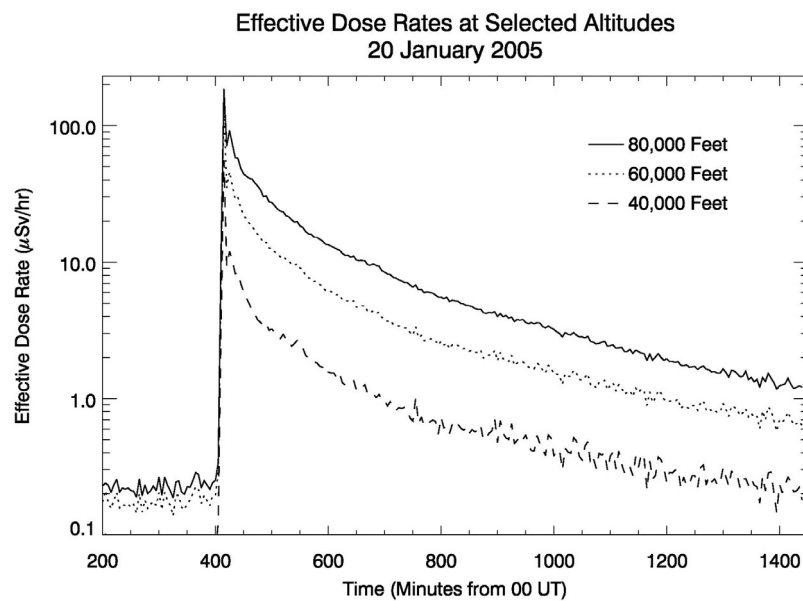
Figure 13: Effective dose rates in μSv/hr for three selected altitudes during the 20 January 2005 solar proton event and ground level event. Peak dose rates were high (over 185 μSv/hr) , however rates this high were short lived as the spectrum softened rapidly.

The spectra in Figure 12 exhibit some troubling discontinuities between rigidities 950 and 1225 MV. This may be a problem with the method used to model the solar proton spectrum. To examine this more closely, several alternative methods for modeling the solar proton spectrum will be introduced. The first makes use of data processing procedures at the SEC which convert the differential fluxes from then GOES spacecraft into integral flux channels.

An Alternate Method for Modeling the Solar Proton Spectrum

An alternative method for approximating the solar proton spectrum was suggested by *Sauer* (25). Using this method will allow comparisons to be made between the two methods, with the goal that this alternate method will provide a smoother spectrum from 950 to 1225 MV, where Figure 12 shows that the original method produces a very discontinuous spectrum.

This alternate method begins with four integral channels (labeled I3, I4, I5, and I7) along with all four of the HEPAD channels (P8, P9, P10, and P11). The energy ranges for the integral channels are listed in Table 5 below. This data, as is the case with the differential particle data, can be obtained from the NGDC (12).

Table 5: Energy ranges for the integral channels of the GOES energetic particle data (25). (Note that for this method, only channels I3, I4, I5, and I7 are used.)

Channel	Energy Range
I1	>1 MeV (Protons/cm^2/sec/str)
I2	>5 MeV (Protons/cm^2/sec/str)
I3	>10 MeV (Protons/cm^2/sec/str)
I4	>30 MeV (Protons/cm^2/sec/str)
I5	>50 MeV (Protons/cm^2/sec/str)
I6	>60 MeV (Protons/cm^2/sec/str)
I7	>100 MeV (Protons/cm^2/sec/str)

The HEPAD channels (with the exception of channel P11) are reported in terms of differential flux, and thus need to be converted to integral flux. To accomplish this, the HEPAD fluxes reported by the SEC need to be converted back to the original

instrument count rates by multiplying each channel by its respective conversion factor
(listed in Table 6 below).

Table 6: Conversion factors for integral proton data for the HEPAD instrument (24).

Channel	Conversion Factor (k)
P8	67.5 (cm^2-str-MeV)
P9	67.5 (cm^2-str-MeV)
P10	162. (cm^2-str-MeV)
P11	1565. (cm^2-str-MeV)

As was the case with the original method described earlier, the background
galactic cosmic ray count rate must be subtracted to obtain the count rate due only to
solar protons. The same method for calculating the background as was described for the
original method is used here.

With the background galactic cosmic ray count rate subtracted, the derivation of
the eight solar proton spectra spanning the eight integral channels can proceed. These
eight spectra are combined, just as in the previous method, to make up the piecewise-
continuous approximation of the entire solar proton spectrum. A full explanation of this
alternate method is given in Appendix B.

In Figure 14 below, the modeled solar proton spectrum using this alternate
method is compared with the solar proton spectrum modeled using the original method.
At rigidities above 1225 MV, the two methods produce nearly identical spectra. Between
950 and 1225 MV, the alternate method just described appears to provide a better
approximation to the actual solar proton spectrum. However, below 950 MV, the

spectrum derived using the alternate method is much more discontinuous than the original method.

Proton Spectrum
20 January 2005
0705 UT
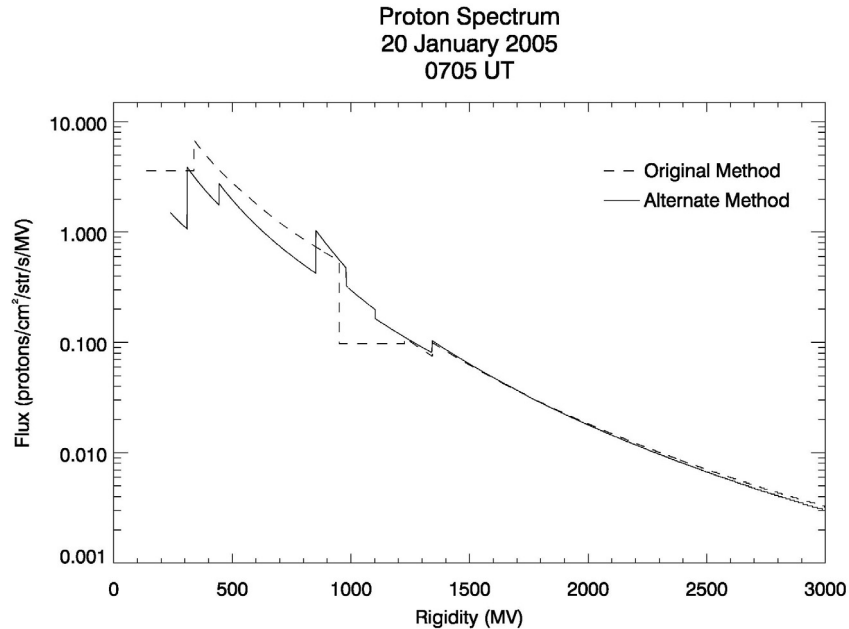
Figure 14: Comparison of the proton spectrum using the original method and the alternate method described above. While the two methods produce nearly identical spectra above 1225 MV, discontinuities are evident with each method below 1225 MV.

Figure 15 shows a comparison of the differential effective dose rates found using both the original method and the alternate method described in this section. The plot shows the rigidity distribution of the effective dose rate for each method, which illustrates where in the rigidity range the bulk of the dose rate comes from. The problem with the original spectrum is manifested as a sharp decrease in the differential dose rate from 950 to 1225 MV. Since the bulk of the dose rate appears to come from the rigidity range from 650 to 1400 MV, the alternate method most likely does a better job of estimating the dose rate since it has an overall smoother approximation of the solar proton spectrum in this rigidity range.

51

Figure 15: Comparison of the differential effective dose rate as a function of rigidity using the original method and the alternate method. The original method exhibits a troubling discontinuity from 950 to 1225 MV. The alternate method displays a more realistic looking differential dose rate across this range of rigidities.

To further illustrate the trouble the original method has in estimating dose rates using the modeled solar proton spectrum, Figure 16 shows the proton spectrum derived using both methods along with the dose rate curve using the original method. It is clear that the large discontinuity in the solar proton spectrum derived using the original method causes an unphysical decrease in the differential dose rate curve. This appears to be a problem with the way the channel P7 flux is being handled. Such a sharp decrease in the proton spectrum cannot be explained physically, and leads to an even more abrupt decrease in the dose rates. This is especially troubling since the bulk of the dose rate appears to come from the range of rigidities spanning 650 to 1400 MV. The proton spectrum derived using the alternate method has less of a discontinuous nature within the rigidity range that contributes the most to the dose rate. There is still, however, a

troubling discontinuity with this alternate method at rigidities lower than 950 MV, which

may lead to errors in dose rates. This discontinuity does not appear to be physical in

nature, but more likely a limitation of the method used to model the proton spectrum.
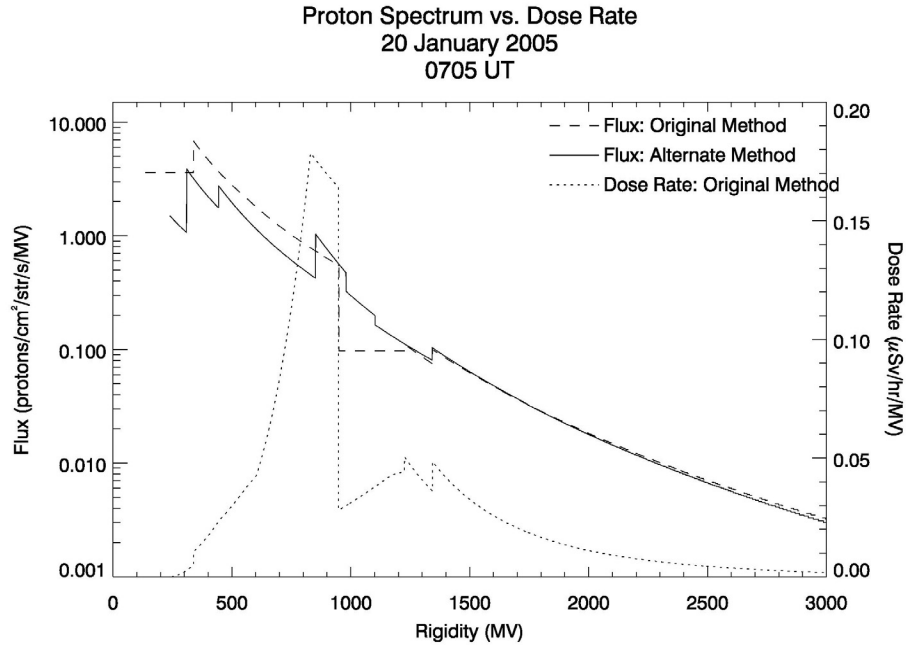
Figure 16: The proton spectra for both methods discussed are shown along with the dose rate for the original method. This highlights the portion of the proton spectrum that provides the largest contribution to the dose rate. The bulk of the dose rate comes from rigidities 650 to 1400 MV.

Although a complete solution to the problem of the discontinuities in the modeled

solar proton spectra cannot be offered at this time, a third method for modeling the proton

spectrum is presented below which attempts to provide a fix to the way in which the

original method approximates the solar proton spectrum. This fix is an attempt to

"connect the dots" between channels P6 and P10 in order to smooth out the proton

spectrum. To perform this correction, the method for correcting the differential flux was

changed (see Chapter III: Correction Factors for GOES Energetic Particle

Measurements). In correcting the differential flux in channel P7, the correction factor

used was nearly an order of magnitude smaller than the correction factors used for the other channels. To smooth out the spectrum, the correction factor used for channel P7 was altered to match the factor used for channel P6 at the lower rigidity limit (950 MV), and the factor used for channel P10 at the upper rigidity limit (1225 MV). This change effectively smoothed out the solar proton spectrum in this region.

Figure 17 below is a comparison of the solar proton spectra at 0705 UT during the 20 January 2005 event modeled using the original method and the revised method, which attempts to smooth out the spectrum along channel P7. It is clear that the revised method matches the original method very well with the exception of the large discontinuity between 950 and 1225 MV.
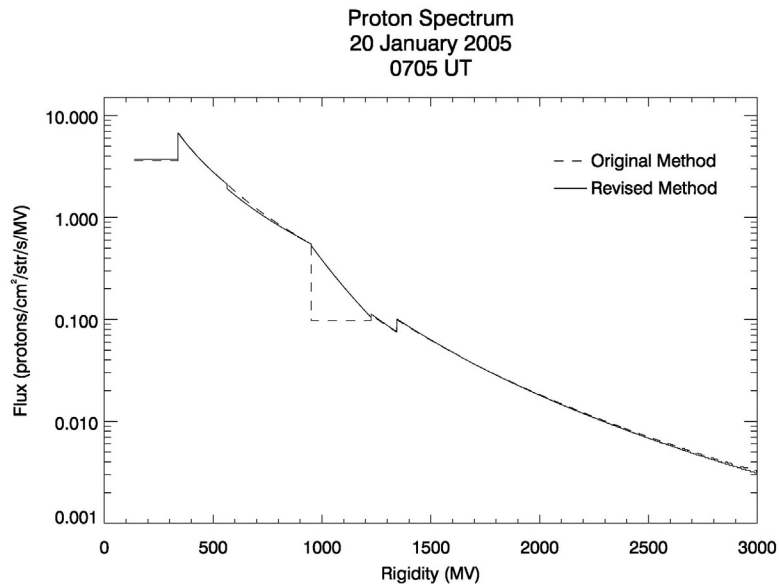
Figure 17: Comparison of the solar proton spectrum using the original method and the revised method to "connect the dots" between rigidities 950 and 1225 MV.

Figure 18 shows a plot of the differential dose rates calculated using the modeled solar proton spectra from the original method and the revised method just described.

54

Again, the discontinuity from 950 to 1225 MV has been smoothed out providing a more realistic curve of the differential dose rate. Integrating these differential dose rates provides a total dose rate of 105.09 μSv/hr for the revised method, compared to 91.80 μSv/hr using the original method. This is a 14.5% increase in the dose rate over the rate estimated by the original method.
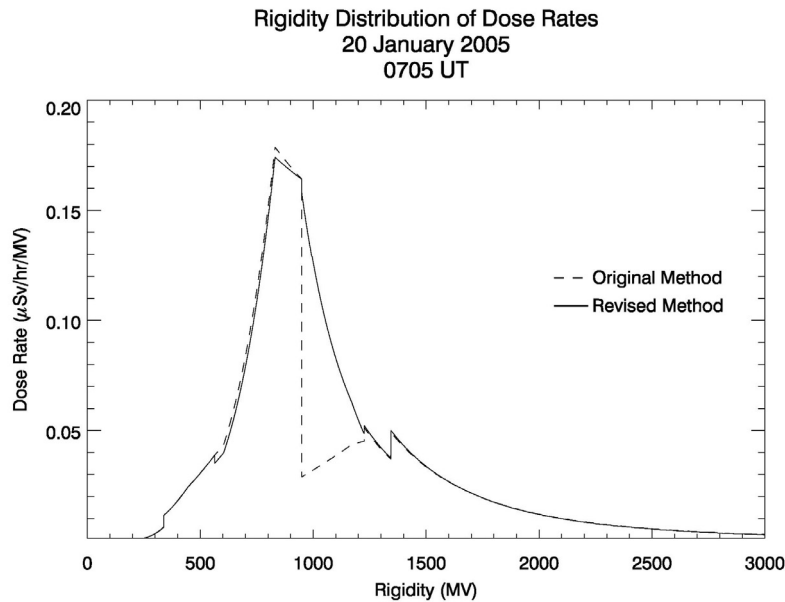
Figure 18: Comparison of the dose rate at 0705 UT using the original method and the revised method described above. The total dose rate (area under the curve) difference between the two methods for 0705 UT is 13.30 μSv/hr.

Finally, Figure 19 shows the modeled solar proton spectra using the original and revised methods, along with the differential dose rate using the revised method to depict where in rigidity the bulk of the dose rate comes from. The fix provided to the solar proton spectrum derived using the original method clearly accounts for a significant portion of the estimated dose rate. The dose rate estimated using the original method was 12.6% below the dose rate derived using the revised method.

Given the more continuous nature of the revised method, and its better handling
of the solar proton flux between 950 and 1225 MV, the revised method appears to
provide the best solution to the problem of approximating the solar proton spectrum and
estimating dose rates at this time.
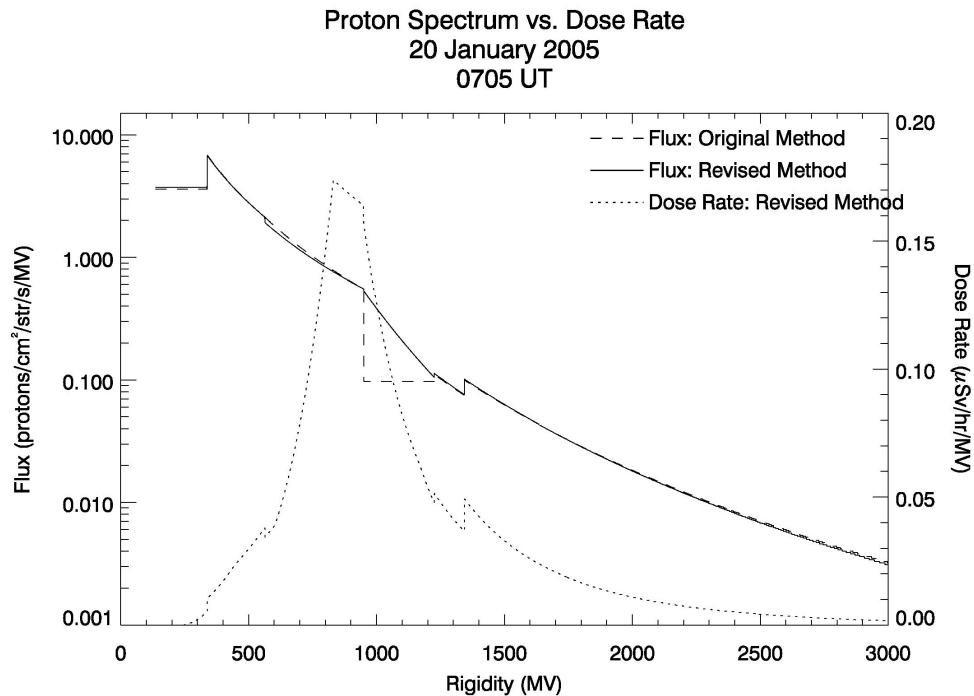
Figure 19: Comparison of the proton spectrum using the original method and the revised method along with the dose rate using the revised method. The peak of the dose rate occurs near 820 MV, but a significant portion falls between 950 and 1225 MV where the original model of the spectrum appears to have trouble.

The dose rates presented above assume that all energetic protons measured by the
GOES Space Environment Monitor make it to the top of the atmosphere where they
produce the secondary particulate flux. This assumption is rarely correct because of the
effects of geomagnetic shielding discussed earlier. The lower in latitude one goes, the
more energetic a particle must be to traverse the earth's geomagnetic field and reach that
location.

Since no particles below the cutoff rigidity will arrive at a particular location, the integration of Eq. (19) should actually start at the cutoff rigidity. This ensures that particles that do not reach the top of the atmosphere are not being counted in the dose rate calculation. These effects will be incorporated into the dose rate calculation in the following section.

Geomagnetic Cutoff Determination

With methods to model the proton spectrum and compute effective dose rates, attention must be given to the problem of geomagnetic cutoff determination. How much does the geomagnetic cutoff rigidity matter? How much does the cutoff rigidity change at a particular location during geomagnetic storming? If changes in geomagnetic cutoff are not significant during a large geomagnetic storm, then accounting for those changes will not prove beneficial. Even if changes in cutoff are significant, will those changes affect the dose rates significantly at particular locations and altitudes? These questions will all be investigated in the following paragraphs.

As mentioned previously, determining geomagnetic cutoff rigidities is a computationally intensive process which must be simplified by using various cutoff search strategies. The goal of a search strategy is to balance the computer time required against the accuracy of the cutoff determination. A typical search begins with very high-energy particles and reduces the energy in fixed steps until the last allowed/forbidden transition is found. This process must be performed for each latitude and longitude of interest, as well as each altitude (if variation in altitude is desired). This approach can be accurate but is very time consuming if the steps are small enough to be accurate. A

bounded search strategy starts with high-energy particles and then takes a big step down in energy to get below the cutoff. Once below the cutoff the process steps back up in energy and gradually reduces the lower and upper bounds to find the cutoff.

Using a geomagnetic cutoff rigidity model developed by *Smart et al.* (27), we can calculate the cutoff rigidity for a single location on the globe. Adding multiple locations slows the process down some, but a world-wide grid of cutoffs with a resolution of 5 degrees in latitude and longitude can be computed in a matter of hours. Using this model, the upper, lower, and effective cutoffs were computed along the 280° East meridian and plotted in Figure 20 below. The cutoff penumbra, located between the upper and lower cutoffs, is easily seen. Comparing this figure with the cutoff penumbra shown in Figure 7 above shows a remarkable consistency. These figures show that the cutoff penumbra collapses at latitudes greater than 50 degrees, or at rigidities below 1 GV, which should make the cutoffs for these latitudes/rigidities easier to compute.

Unfortunately, this model does not allow the simulation of geomagnetic storming which may alter the cutoffs significantly. To incorporate geomagnetic storming effects, the cutoff model must incorporate the complex current systems which exist in the magnetosphere along with the geomagnetic field model. The charging of these current systems during geomagnetic storms is responsible for changes to the geomagnetic field, which alter the cutoff rigidity.

For this study, cutoff rigidity effects were incorporated through the use of a FORTRAN program designed to calculate the cutoff rigidity at a certain energy and location using the International Geomagnetic Reference Field (IGRF) epoch 2000 and the

Tsyganenko 1989 (7) magnetospheric model. The program was developed by the

University Partnering for Operational Support (UPOS) and is available to the public for

download (38). The inclusion of the Tsyganenko 1989 magnetospheric model is

important because it accounts for the currents that exist in the magnetosphere, allowing

the simulation of geomagnetic storming through manual alteration of the Kp index. As

was described earlier in Chapter II: Solar Energetic Particles, the Kp index is a global

measure of geomagnetic activity.
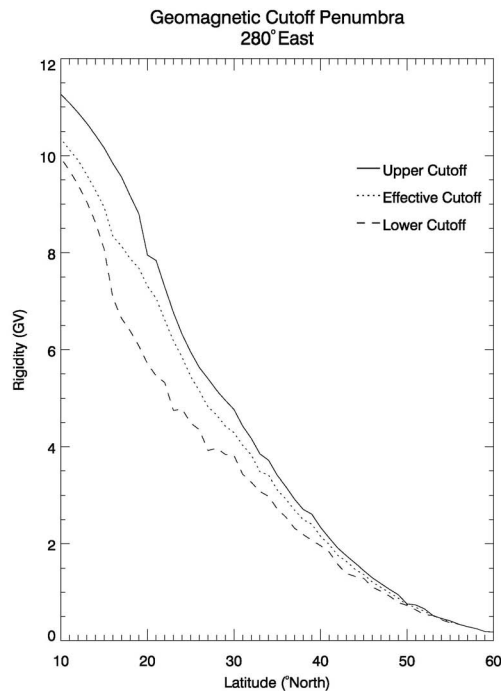
Figure 20: Geomagnetic cutoff penumbra along the 280° East meridian. Note that the size of the penumbra increases as latitude decreases and rigidity increases. Below approximately 1 GV in rigidity, or higher than 50° in latitude, the cutoff penumbra decreases rapidly in width.

The search strategy used by this program is different from that used in the *Smart*

et al. cutoff rigidity program (27) in that it iterates through latitude at a fixed energy

instead of the other way around. For a particular energy, and along a specific meridian,

the program steps through latitudes from low to high until an escaping trajectory is found.

The program then repeats along a different meridian until a circle around the globe has been made at a constant energy. The energy is then changed and the process is repeated. An example of the output produced by this program is shown in Figure 21 below. The program was run for an energy of 1000 MeV which corresponds to a rigidity of 1696 MV. The cutoffs were calculated along meridians every 30 degrees beginning with the zero degree meridian.
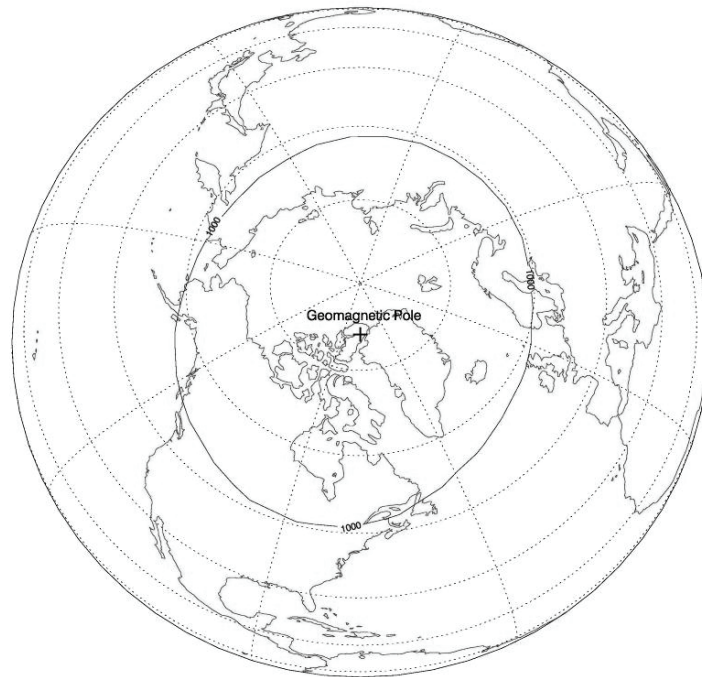
Figure 21: Depiction of the 1000 MeV (1696 MV) geomagnetic cutoff location in the northern hemisphere. The plot was created using the UPOS program designed to compute geomagnetic cutoffs by keeping energy constant and iterating through latitudes.

This geomagnetic cutoff program can be used to investigate changes in cutoffs due to changes in geomagnetic activity, changes in longitude, and diurnal changes. To investigate the effect that a geomagnetic storm has on cutoffs, the UPOS program was run with a Kp index of 0 to simulate quiet geomagnetic conditions, and again with a Kp

index of 6 to simulate geomagnetic storm conditions. The version of the UPOS program used in this paper uses the Tsyganenko 1996 magnetospheric model, which allows Kp inputs ranging from 0 to 6. Output from these two simulations were used to create Figure 22 below. At low energies, changing the Kp index significantly (from 0 to 6) causes the cutoff latitude to change by as much as 5 degrees. Indeed, research conducted by *Smart et al.* (26:6) indicates that geomagnetic storming characterized by a Kp index of 9 would allow as much as a 10 degree shift in geomagnetic cutoff latitude for particle energies up to 1 GeV. Note that in Figure 22, the cutoff differences between active and quiet geomagnetic conditions decrease as energies approach 5 GeV. This suggests that geomagnetic activity does not cause a significant variation in the cutoffs for high energies or low latitudes.

The next discussion concerns the longitudinal dependence of the geomagnetic cutoffs. Figure 23 shows that longitudinal differences can cause changes in cutoff latitudes as well, sometimes by as much as 7 degrees. These longitudinal effects are regular in nature though and can be explained by the offset of the geomagnetic pole from true north. The greatest variation occurs along the meridian where the geomagnetic pole is currently located. In the northern hemisphere, this is at 288.2° East (71.8° West), and in the southern hemisphere, this is at 108.2° East (251.8° West). Figure 23 shows that for the northern hemisphere, longitudes near 280° East have the lowest cutoff rigidities. This is because the north geographic pole is shifted equatorward by 10.3° along the 288.2° East meridian. Similarly, longitudes near 80° East in the northern hemisphere have the highest cutoff rigidities because the 80° East meridian is opposite the 280° East meridian.

Geomagnetic Cutoff Energies (MeV)
Over the North and South Geomagnetic Poles
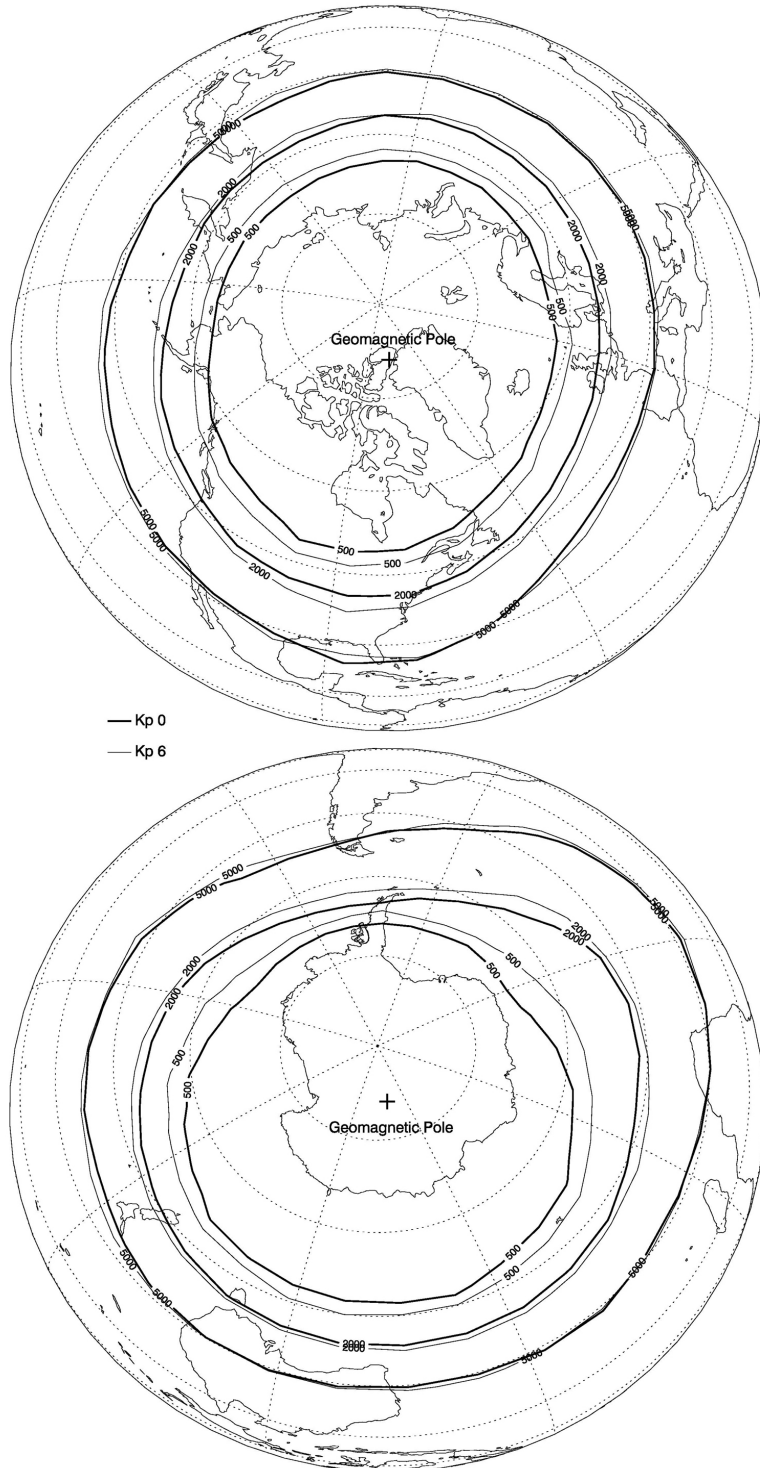
Figure 22: Geomagnetic cutoffs in the northern / southern hemispheres under different levels of geomagnetic activity. Bold ovals indicate cutoffs at the specified energies (MeV) for quiet geomagnetic conditions (Kp=0); thin ovals indicate cutoffs for active geomagnetic conditions (Kp=6).
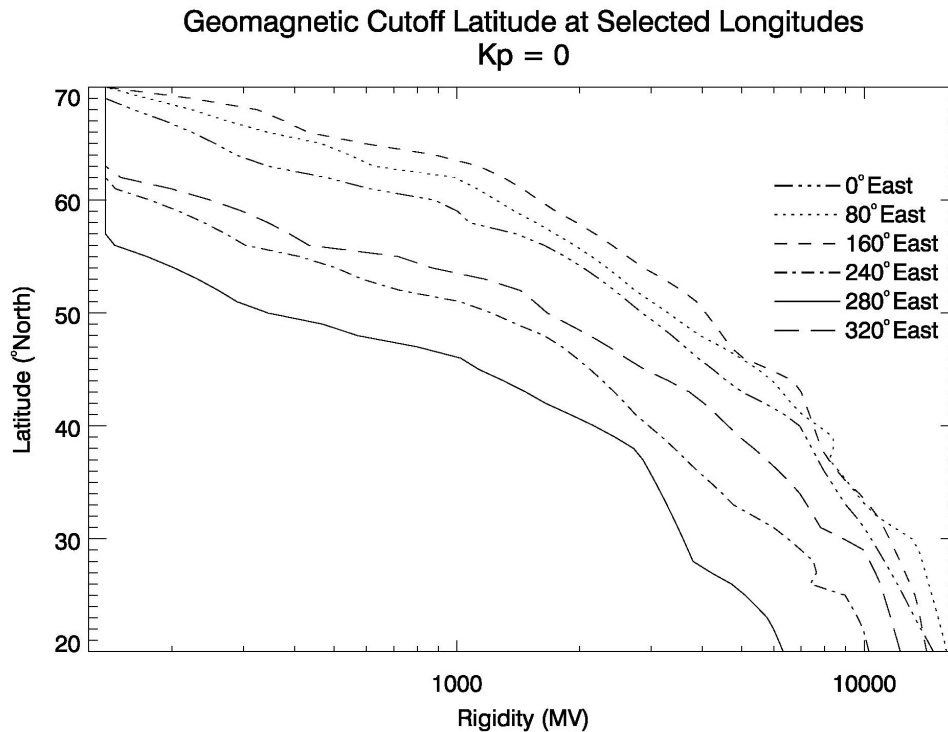
Figure 23: Geomagnetic cutoffs calculated along selected longitudes. The lowest cutoff is in the vicinity of 280° East. This is because the north geomagnetic pole is currently located near 288° East. A similar effect is seen in the southern hemisphere near 108° East.

The last parameter to investigate is the diurnal dependence of the geomagnetic cutoffs. Figure 24 depicts the cutoffs along the zero degree meridian at two times, 12 hours apart. The zero degree meridian was selected because it provided the largest diurnal difference in cutoffs. Other longitudes examined showed less variation. It is clear that the diurnal differences are negligible when compared to the larger differences caused by position and geomagnetic storming effects. Therefore it is a reasonable approximation to ignore the diurnal differences in geomagnetic cutoff.

This figure also emphasizes the point made earlier in Figure 22 that geomagnetic activity affects the cutoffs the most at rigidities less than approximately 5000 MV or latitudes greater than approximately 45°. At higher energies and lower latitudes, the level

of geomagnetic activity, characterized by the Kp index in the figure, does not cause a significant change in the cutoff.

With this in mind, the cutoff program can be run using Kp indices to simulate different levels of geomagnetic storming. This will allow the creation of a world-wide grid of cutoffs for each Kp index which can be used to determine the cutoff for any location during any level of geomagnetic activity.
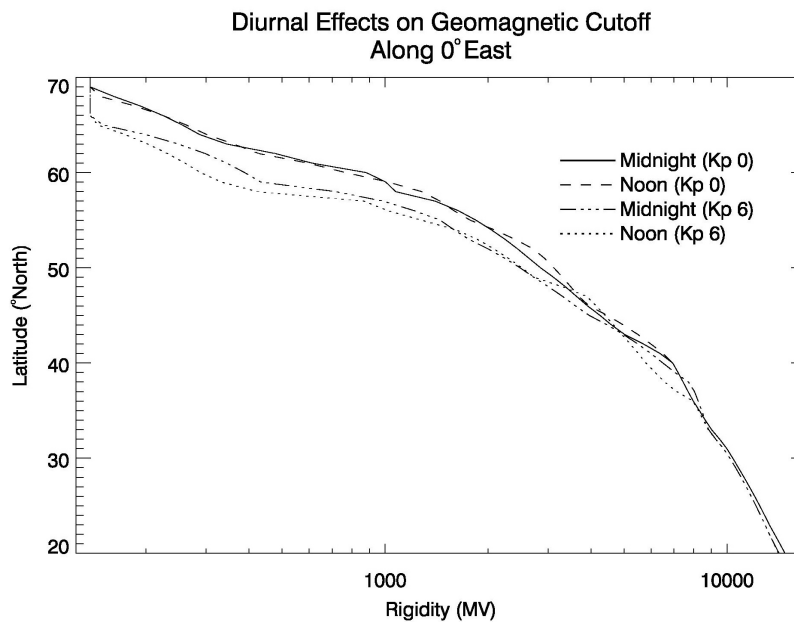
Figure 24: Diurnal changes in geomagnetic cutoff rigidity as compared to magnetic storming effects. The differences are slightly larger for the Kp 6 data, indicating that the diurnal changes are slightly larger during periods of strong geomagnetic activity. Cutoffs were calculated along the 0° East meridian. Other longitudes showed less variation.

The next question to ask is, "Where in rigidity does the bulk of the dose rate come from?" If the bulk of the dose rate comes from high energies (above 5 – 10 GeV, see Figure 22 above), then the level of geomagnetic activity will not have as much effect on the cutoff because the energies which produce most of the dose rate are not affected (as shown in Figures 22 and 24). Figure 18 above shows that the bulk of the dose rate comes

from a rigidity range of approximately 650 to 1400 MV (203 to 747 MeV). Looking at this energy range in Figure 22, it is clear that the level of geomagnetic activity will have a significant impact on the cutoff rigidities we are interested in.

For the calculations in this paper, the atmosphere is assumed to extend to an altitude of 100 km above the surface of the earth. Thus, cutoff rigidities will be calculated for particles incident at an altitude of 100 km. This altitude was chosen because the calculations carried out by *Copeland et al.* (1:2) were performed for particles incident in the atmosphere at 100 km.

Due to the search method employed by the UPOS geomagnetic cutoff algorithm, the lower geomagnetic cutoff rigidity (R_L) is used. Although ignoring the penumbral effects on cutoff rigidity is not ideal, the simplification is not entirely bad since choosing the lowest value for the cutoff will provide the worst-case scenario for the dose rate computations. The effects this simplification has on actual cutoffs will be discussed later in Chapter III: Assumptions Employed and Known Sources of Error.

To create the world-wide grid of cutoff rigidities which will be used to calculate dose rates, an interpolation function was used to create cutoff rigidities along selected meridians at 1 degree latitude spacing, from 20 degrees to 70 degrees. Latitudes higher than 70 degrees are within the polar cap where cutoff rigidities are so low that all solar protons of interest (rigidity greater than 137 MV – see Table 4) are expected to reach an altitude of 100 km. Latitudes below 20 degrees are so low that only particles of extremely high rigidity can penetrate to the atmosphere. These are extremely rare for solar proton events and don't contribute significantly to the effective dose accrued. A

linear interpolation was chosen because of errors introduced by higher-order interpolations.

To simplify the cutoff search process, only vertical trajectories were used. This is a common assumption made since it greatly reduces trajectory computation time (5:193). Assuming purely vertical trajectories is a good approximation to make if the scale size of the gradient in the earth's magnetic field is less than the gyroradii of the particles (27:7). The validity of this assumption and other assumptions made are discussed in the next section.

Assumptions Employed and Known Sources of Error

In modeling the spectrum of rigidities during solar proton events and then calculating effective dose rates for specified locations and altitudes around the earth, certain assumptions and simplifications must be made. The quicker the calculation must be made, the more simplifications will be required to speed up the computations. There is a trade-off that must be reached between the timeliness of the calculations and the precision required. Assumptions and simplifications that have been made in the processes outlined above are now discussed.

The first assumption being made in this process is that the particles being measured by the GOES spacecraft are representative of the particle flux everywhere around the globe at that time. This is not always the case. Solar proton events are usually anisotropic in nature when they begin. Particles traveling along field lines between the sun and the earth will arrive first, meaning the flux will not be isotropic. Over time however, the solar wind and the interplanetary magnetic field cause bending

and scattering in the trajectories of the particles, and the flux eventually becomes much more isotropic. The time required for the flux to take on isotropic characteristics depends on the properties of the solar wind, the interplanetary magnetic field, and the nature of the accelerated particles.

The process for modeling the solar proton spectrum first described by *Copeland et al.* (1) uses the GOES Space Environment Monitor's channel P11 to describe the integral proton flux for energies greater than 700 MeV. However, the calculation of the spectral hardness which describes this range of energies is made using information from the previous channel (P10). Thus, an assumption is being made that the form of the proton spectrum determined by satellite measurements of energies up to 700 MeV is also valid at higher energies (15:76). Without additional instrumentation, this is a difficult assumption to check. However, as will be shown in the Results and Analysis section below, the bulk of the dose rates caused by most solar proton events comes from energies less than about 830 MeV (1500 MV). So the extrapolation of the energy spectrum to energies greater than 700 MeV will not ordinarily cause a large amount of uncertainty in the calculations.

When calculating geomagnetic cutoff and modeling proton interactions with the atmosphere, the assumption was made that the atmosphere extends to a height of 100 km above the surface of the earth, and that no particle interactions take place until the solar protons reach this boundary. This allows us to use 100 km as the altitude at which to compute the geomagnetic cutoff. This is also the altitude that was input into the MCNPX 2.4.0 code which was used to convert particle fluences to effective dose rates per unit flux. As was mentioned earlier in Chapter III: Effective Dose Calculation, the

atmospheric pressure density at 100 km is low enough (approximately 0.0003 g/cm^2 (12))

that accounting for the additional atmosphere between 100 km and the GOES orbit would

not significantly improve the dose rate estimates (1:2).

In computing the geomagnetic cutoffs, particle trajectories that were not vertically

incident were ignored. This greatly simplified the geomagnetic cutoff calculations which

are the most computationally intensive part of this process. Previous studies have shown

that the earth's magnetic field has a "focusing effect," such that particle trajectories that

are not vertically incident reached a similar final asymptotic direction at great distances

from the earth (27:7). As mentioned earlier, this is a good approximation to make if the

scale size of the gradient in the earth's magnetic field is less than the gyroradii of the

particles. In the case of solar proton events, the particles leading to increased dose rates

in the earth's atmosphere have been accelerated to relativistic energies. The gyroradius

of a 100 MeV proton at geosynchronous orbit is approximately 1.4×10^4 km. The scale

length of the gradient in the earth's magnetic field is approximately 6.96×10^3 km at this

location. So the gyroradius of a 100 MeV proton is nearly an order of magnitude larger

than the scale size of the gradient of the magnetic field, and therefore, the gyroradii of all

particles with energies greater than 100 MeV are large enough to safely assume that the

particles are incident in the vertical direction.

The UPOS geomagnetic cutoff program which was used to calculate cutoff

latitudes for specified energies searched for and found the lower bound of the cutoff

penumbra (R_L). Using this lower bound as the actual geomagnetic cutoff in Eq. (19) may

lead to an overestimation of the dose rate. However, Figure 20 shows that this

overestimation would only occur at rigidities greater than approximately 1500 MV (830 MeV) or at latitudes below approximately 45°. This is because at lower rigidities or higher latitudes the cutoff penumbra shrinks rapidly, making the lower cutoff essentially the same value as the effective and upper cutoffs. As will be shown in Chapter IV: Results and Analysis, this is not a significant source of error for most solar proton events because the bulk of the radiation dose comes from protons with rigidities below 1500 MV. One exception was the onset of the 20 January event where, due to the extreme hardness of the spectrum, protons with rigidities in excess of 2000 MV contributed significantly to the dose rates.

In order to calculate the geomagnetic cutoff, the UPOS program incorporates a geomagnetic field model. The simulations run for this study made use of the IGRF epoch 2000 for the earth's geomagnetic field, and the Tsyganenko 1989 magnetospheric model to simulate current systems in the magnetosphere. The IGRF 2000 field provides a significant improvement over simply using a pure dipole field (19), however it is important to note that the IGRF is updated every couple of years due to slight variations in the geomagnetic field over time. Therefore, it is important to use the version of the IGRF nearest to the time period of the event being studied. The Tsyganenko 1989 model allows manipulation of the Kp index to simulate various levels of geomagnetic storming. The Kp index is allowed to vary from 0 to 6 in the version of the model used for this study. However, the model does not show the effects of the magnetopause compression during active conditions, which would cause a further decrease in geomagnetic cutoff rigidities during strong geomagnetic storms (19).

A significant source of error may come from the method in which incident high-energy protons are converted to effective doses in tissues. The radiation weighting factors listed in Table 1 have undergone frequent revision in the past (17:280) and the process by which effective dose rates are calculated from a given proton spectrum is not straightforward. Depending on the path the secondary particles take through the body being irradiated (AP, PA, LAT, or ISO – see Chapter II) the coefficients used to calculate effective dose rates per unit fluence may change by up to a factor of four (17:A1.7).

IV. Results and Analysis

Chapter Overview

This chapter covers the results produced using the methods described above. First, several historical events are discussed, calculated dose rates for each event are presented, and comparisons between the events are made. Next, comparisons are made between dose rates computed with and without taking into account geomagnetic cutoff effects. Then, comparisons are made to results produced by the CARI-6 algorithm which does not take into account solar proton events. Finally, the limited data gathered from instruments onboard aircraft is presented for comparison with model results from this study.

The 14 July 2000 "Bastille Day" Event

The 14 July 2000 "Bastille Day" event was the result of a strong X5 solar flare which occurred at 1024 UT. An image of this flare taken by the Solar Heliospheric Observatory (SOHO) is shown in Figure 25 below. The white enhancement in the center of the solar disk shows the location of the flare. The horizontal white line is an artifact in the image. Energetic particles associated with this event that reached the earth caused widespread communications disruptions, problems with satellite operations, and even isolated power grid failures (35). The results presented in this section do not account for geomagnetic cutoff effects.

The solar protons accelerated by this event began to arrive approximately 20 minutes after the onset of the X-ray flare, with the maximum energetic particle flux

occurring at 1230 UT (just over two hours after the flare). The maximum energetic

particle flux is defined as the largest flux of particles with energies greater than 10 MeV.

The dose rates caused by this event peaked at 1200 UT, which was 96 minutes after the

flare onset.
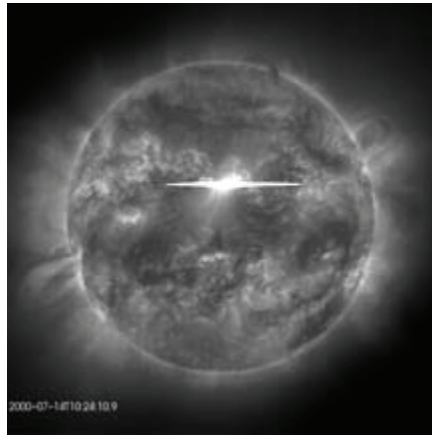
Figure 25: Image from the Solar Heliospheric Observatory's Extreme Ultraviolet Telescope taken at 1024 UT on 14 July 2000. The white enhancement in the center of the image shows the location of the flare. The horizontal white line is an artifact produced by an overload of energy on the imaging sensor (35).

The solar proton spectrum estimated at three different times is shown in Figure

26. The times 1200 UT and 1210 UT were chosen to capture changes in the solar proton

spectrum at and immediately following the dose rate peak (which occurred at 1200 UT);

1600 UT was chosen to show the evolution of the spectrum after 4 hours. Initially, the

proton spectrum indicates that the flux decreases with increasing rigidity, as expected. At

1200 UT, the solar proton spectrum was at its hardest. This corresponds to the same time

that the maximum dose rate was produced. The solar proton spectra and dose rates

presented below were all calculated using the revised method described in Chapter III.

All dose rate calculations were made using an altitude of 80,000 ft unless otherwise noted.
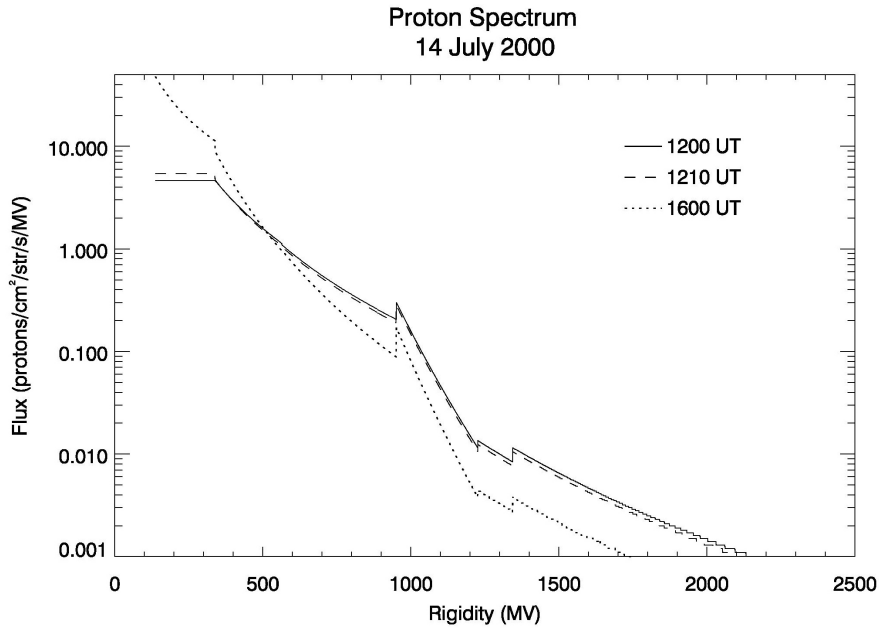
Figure 26: Solar proton spectra plotted as differential flux (on a log scale) as a function of rigidity at 1200 UT, 1210 UT, and 1600 UT on 14 July 2000.

Figure 26 above shows that the solar proton spectrum at 1210 UT (10 minutes after the peak dose rate) has softened, although only slightly. The flux of particles with rigidities greater than 500 MV has decreased while the flux of particles with rigidity less than approximately 340 MV has increased. The dose rate at 1200 UT was 32.97 μSv/hr, while the dose rate 10 minutes later was 30.93 μSv/hr. This shows that the dose rate decreased by 2.03 μSv/hr, or 6.2%, at 80,000 ft from 1200 to 1210 UT, coincident with the softening of the spectrum. However, the >10 MeV particle flux increased by 129.75 protons/cm^2/sec/str, or 7.7%, during this time. The reason the dose rate decreased despite an increase in the flux is because the rigidities which contribute the most to the dose rate

are located between 300 and 1500 MV (see Figure 27), and most of this portion of the spectrum actually decreased as shown in Figure 26.

Four hours later (1600 UT), the solar proton spectrum in Figure 27 has softened further. The rigidities which contribute the most to the dose rate decreased, leading to a dose rate at 1600 UT of 20.37 µSv/hr, or a 38.2% decrease over 4 hours. The >10 MeV flux at 1600 UT increased by 3798.40 protons/cm^2/sec/str, or 224.9%, over the flux recorded at 1200 UT. This shows that the spectral hardness plays a very important role in determining the amount of dose produced by incoming solar protons.
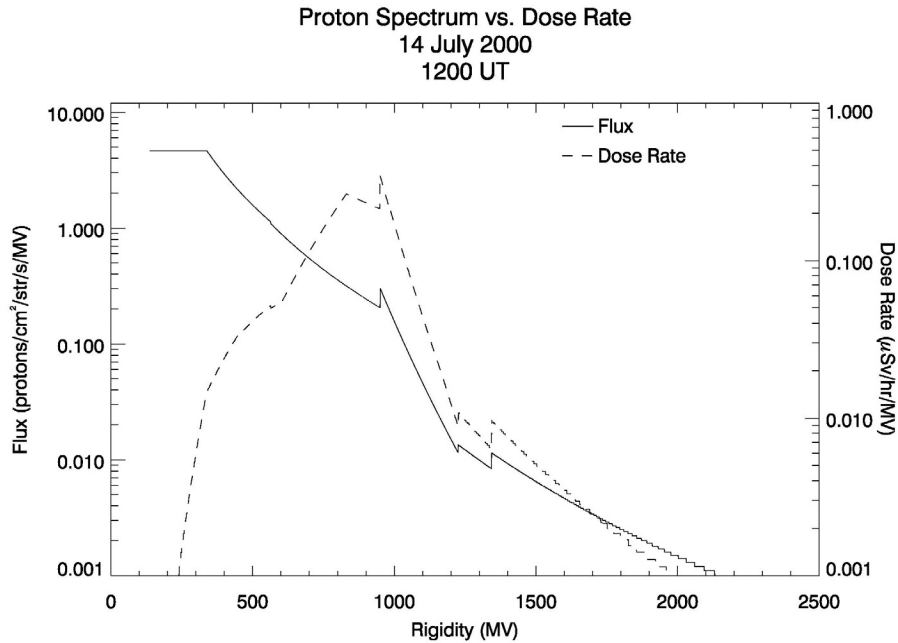
Figure 27: Solar proton spectrum shown as differential flux (log scale) vs. rigidity, and associated differential effective dose rate (log scale) at 1200 UT on 14 July 2000 at 80,000 ft. The greatest contribution to the dose rate comes from the rigidity range 300 to 1500 MV.

Figure 28 shows differential effective dose rates at three selected times, and how they change over time. There is not much change in the first 10 minutes of the event, with total dose rates decreasing by only 6.2%. This is expected since there was not a

significant change in the spectra for these times shown in Figure 26 above. At 1600 UT however, the total dose rate has decreased by 38.2% since 1200 UT, and the rigidities contributing to the dose rate have decreased as well. This is due to the softening of the proton spectrum, with fewer energetic particles being observed that contribute significantly to the effective dose rate at 80,000 ft.
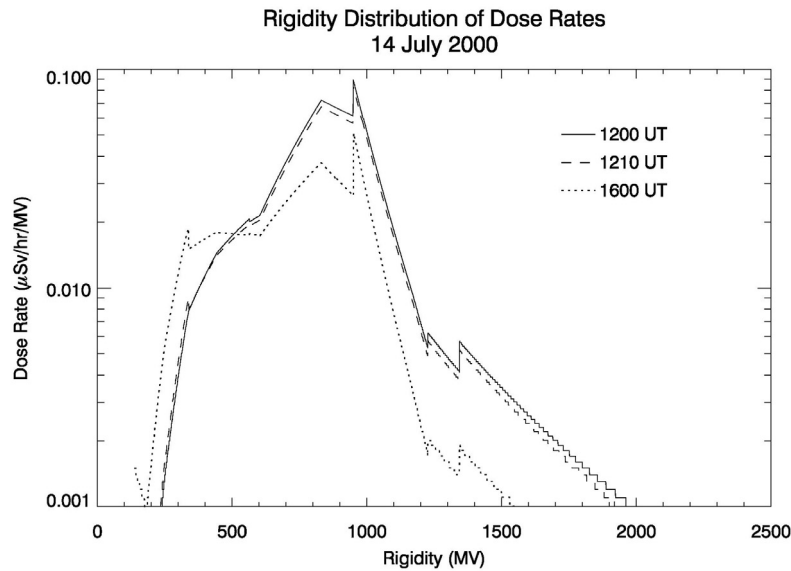
Figure 28: Differential effective dose rates (log scale) vs. rigidity due to solar protons at 1200 UT, 1210 UT, and 1600 UT on 14 July 2000 at 80,000 ft. Integrating the differential dose rates shown gives total effective dose rates of 32.97 μSv/hr at 1200 UT, 30.93 μSv/hr at 1210 UT, and 20.37 μSv/hr at 1600 UT.

Figure 29 below shows the effective dose rates at three selected altitudes as a function of time. At approximately 1035 UT (635 minutes from 00 UT), the dose rates at all three selected altitudes begin to increase. This marks the initial arrival of the energetic particles accelerated by the flare. The maximum dose rate is not reached until approximately 85 minutes later (at 1200 UT, or 720 minutes from 00 UT). Again, the maximum dose rate corresponds to the hardest spectrum. Dose rates then decrease as the spectrum softens despite an increase in flux of lower energy particles.
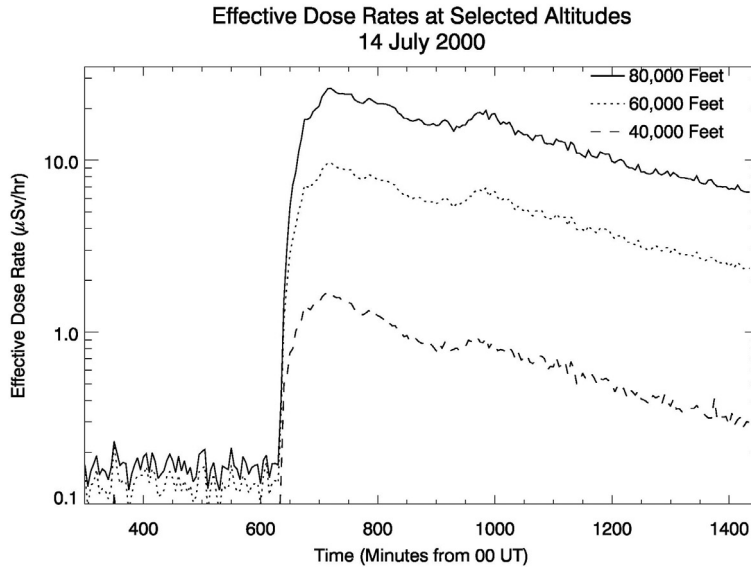
Figure 29: Effective dose rates (log scale) over time at three selected altitudes as a function of time during the 12 July 2000 solar proton event.

Total doses accrued over hypothetical flights of duration 1, 3, 5, and 10 hours are shown in Table 7 below. These hypothetical flights began at the maximum dose rate (1200 UT), and were estimated for an altitude of 80,000 ft. The dose rates initially are not significant, contributing to only 0.15% of the FAA recommended annual limit of 20 mSv in the first hour. However, a 10 hour accrued dose of 180.8 µSv contributes almost 1% of the recommended annual limit, and this does not include any contribution from galactic cosmic rays. Geomagnetic cutoff effects have not been taken into account.

Table 7: Total effective doses accrued over specified flight times at 80,000 ft during the 14 July 2000 solar proton event. Hypothetical flights began at the time of the peak dose rate – 1200 UT.

Total Effective Accrued Doses			
1 hour	3 hours	5 hours	10 hours
30.0 µSv	76.5 µSv	116.0 µSv	180.8 µSv

The 20 January 2005 Event – Largest GLE in 50 Years

The 20 January 2005 was an extremely rare event in that it produced the largest GLE recorded in over 50 years. Although not associated with an unusually large solar flare (the event was caused by an X7 solar flare at 0636 UT), the location of the flare in the sun's western hemisphere was most likely directly connected to the Earth via magnetic field lines. The initial flux was extremely hard, with the spectral hardness softening somewhat with time. The results presented from this event below do not account for geomagnetic cutoff effects.

The energetic particles associated with this event began to arrive within 15-20 minutes after the X-ray flare, with the maximum energetic particle flux occurring at 0710 UT (only 34 minutes after the flare). The maximum energetic particle flux is defined as the largest flux of particles with energies greater than 10 MeV. The dose rates caused by this event peaked at 0655 UT, only 19 minutes after the flare onset, indicating that the protons were of very high energy to arrive that quickly.

The proton spectra shown in Figure 30 indicate a much harder flux than previous plots have shown. At 0655 UT, particles with rigidities of nearly 21 GV were observed, which is considerably higher than 4 GV, which was the maximum rigidity for particles in the 14 July event. Figure 31 shows the solar proton spectrum for the 20 January event at rigidities greater than 1500 MV. Even at 4 hours past the 20 January event peak, particles with rigidities up to 4.5 GV were observed. The hardness of the spectrum for the 20 January event resulted in significantly higher dose rates as compared to the 14 July event.
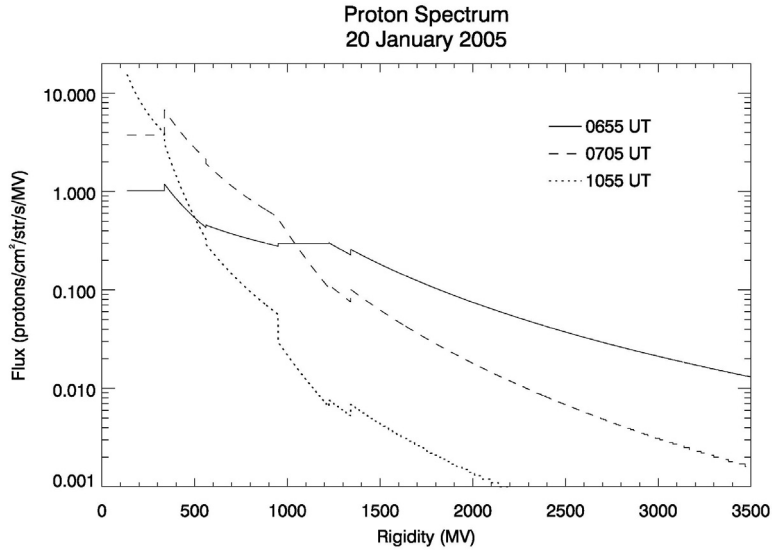
Figure 30: Solar proton spectra plotted as differential flux (on a log scale) as a function of rigidity at 0655 UT, 0705 UT, and 1055 UT on 20 January 2005.
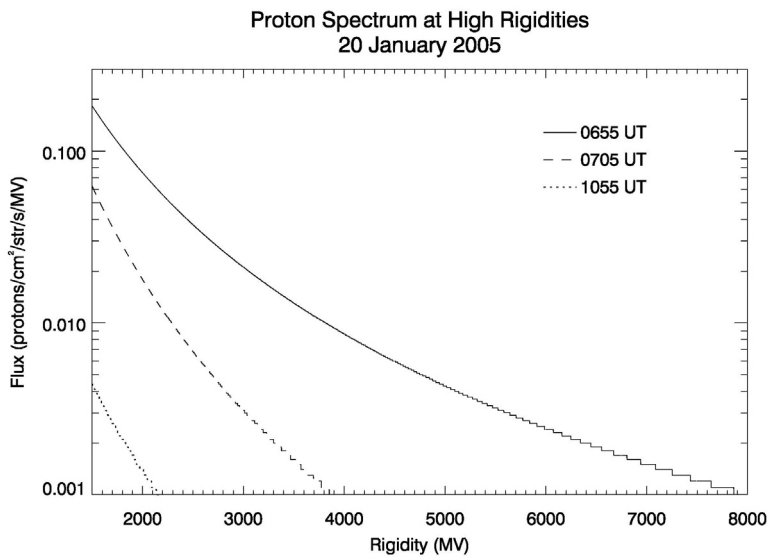
Figure 31: Solar proton spectra plotted as differential flux (on a log scale) as a function of rigidity for values greater than 1500 MV at 0655 UT, 0705 UT, and 0855 UT on 20 January 2005.

The solar proton spectrum of the 20 January 2005 event was at its hardest at 0655 UT, and this also corresponds to the time that the maximum dose rate was produced (the same was true for the 14 July 2000 event). The solar proton spectra and dose rates

78

presented below were all calculated using the revised method described in Chapter III. All dose rate calculations were made using an altitude of 80,000 ft unless otherwise noted. 0655 UT and 0705 UT were again chosen to capture changes in the solar proton spectrum during and immediately following the peak dose rate. 1055 UT was chosen to show how the spectrum had changed in 4 hours.

The proton spectrum measured 10 minutes after the peak dose rate (0705 UT) had softened considerably, as seen in Figure 30. The flux of particles with rigidities above 1100 MV decreased while the flux of particles with rigidity below 1100 MV increased. The dose rate at 0655 UT was an incredible 184.02 µSv/hr, while the dose rate 10 minutes later was 105.09 µSv/hr. The dose rate decreased by 78.93 µSv/hr, or 42.9%, at 80,000 ft from 0655 to 0705 UT. However, the >10 MeV particle flux increased by 1357.87 protons/cm^2/sec/str, or 174.1%, during this time. The reason the dose rate decreased despite a significant increase in the flux is because the rigidities which contribute the most to the dose rate are located between 400 and 7000 MV (see Figure 32), and the bulk of this portion of the spectrum actually decreased (Figure 30).

Four hours later (1055 UT), the spectrum shown in Figure 30 softened further. The flux of particles with rigidities that contribute the most to the dose rate decreased, leading to a dose rate at 1055 UT of 10.59 µSv/hr at 80,000 ft. This is a 94.2% decrease in the dose rate over the 4 hours period. The >10 MeV particle flux at 1055 UT increased by 1059.94 protons/cm^2/sec/str over the flux recorded at 0655 UT, which is a 136% increase. This establishes that the spectral hardness plays a very important role in determining the amount of dose produced by incoming solar protons.
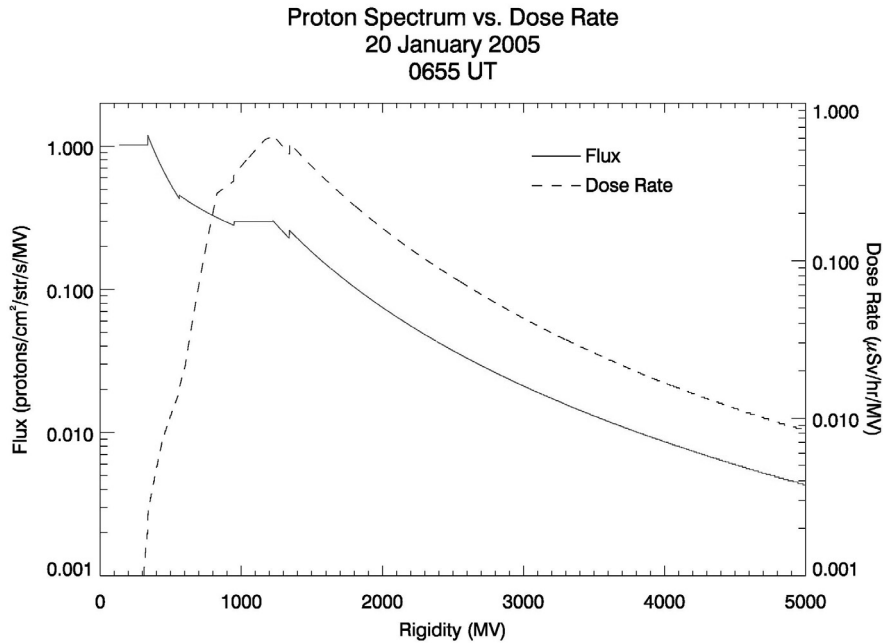
Figure 32: Solar proton spectrum shown as differential flux (log scale) vs. rigidity, and associated differential effective dose rate (log scale) at 0655 UT on 20 January 2005. The greatest contribution to the dose rate comes from the rigidity range 400 to 7000 MV.

Figure 33 shows the differential effective dose rates and how they change over time for the 20 January event. Unlike the previous two events discussed, there is a significant change in the first 10 minutes of the event, with the total dose rate decreasing by 42.9%. Given the large change in the solar proton spectrum shown in Figure 30 above, this does not seem unusual. A significant decrease in the rigidity range contributing the most to the dose rate is also evident. At 1055 UT the total dose rate has decreased by 94.2% over the 4 hour period, and the rigidities contributing to the dose rate continue to decrease as well. This is due to the softening of the proton spectrum, with fewer energetic particles being observed that contribute to the effective dose rate at 80,000 ft.
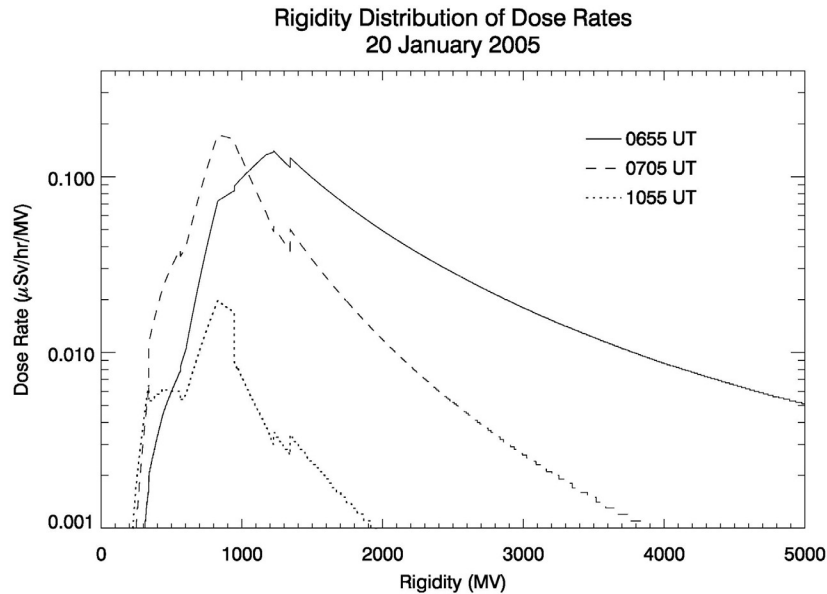
Figure 33: Differential effective dose rates (log scale) vs. rigidity due to solar protons at 0655 UT, 0705 UT, and 1055 UT on 20 January 2005 at 80,000 ft. Integrating the differential dose rates shown gives total effective dose rates of 184.02 μSv/hr at 0655 UT, 105.09 μSv/hr at 0705 UT, and 10.59 μSv/hr at 1055 UT.

Figure 34 below shows effective dose rates at three selected altitudes as a function of time. At approximately 0650 UT (410 minutes from 00 UT), the dose rates at all three selected altitudes begin to increase. This marks the initial arrival of the energetic particles accelerated by the flare (only 16 minutes after the flare!). The maximum dose rate is reached 5 minutes later (0655 UT, or 420 minutes from 00 UT). Again, the maximum dose rate occurred when the proton spectrum was the hardest. Dose rates then decrease as the spectrum softens despite an increase in flux of lower energy particles. The arrival of the solar protons was so soon after the initial acceleration mechanism that they would be expected to have significantly large energies. The particles would need to be accelerated to relativistic speeds to reach the earth that quickly. Indeed, this is what was observed.

81

Effective Dose Rates at Selected Altitudes
20 January 2005
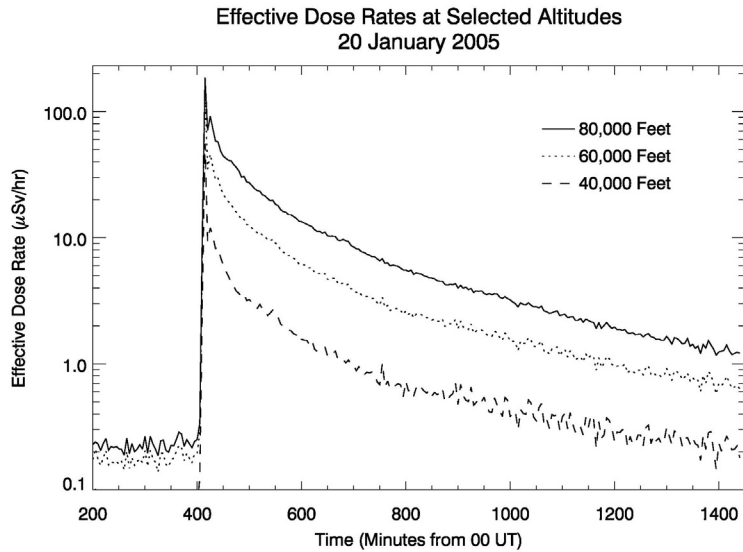
Figure 34: Effective dose rates (log scale) over time at three selected altitudes during the 20 January 2005 solar proton event.

Total doses accrued over hypothetical flights of duration 1, 3, 5, and 10 hours are shown in Table 8 below. These hypothetical flights began at the time of the maximum dose rate (0655 UT), and were calculated for an altitude of 80,000 ft. The dose rates initially are significant, contributing nearly 1%/hr of the FAA recommended annual limit of 20 mSv at the peak of the event. However, because the rates decreased so quickly after the event peak, a 10 hour accrued dose still only contributes about 1% of the recommended annual limit. These values still do not include any contribution from galactic cosmic rays, nor have geomagnetic cutoff effects been taken into account.

Table 8: Total effective doses accrued over specified flight times at 80,000 ft during the 20 January 2005 solar proton event. Hypothetical flights began at the time of the peak dose rate – 0655 UT.

Total Effective Doses Accrued			
1 hour	3 hours	5 hours	10 hours
76.5 µSv	128.3 µSv	153.3 µSv	181.4 µSv

82

Event Comparisons

By comparing the two events discussed above, conclusions can be drawn about the types of events that produce the largest radiation dose rates. This will provide valuable information about the types of events that must be avoided, as well as the types of events that require further study.

The two key factors that affect the total dose accumulation are the magnitude of the peak dose rates, and the duration of the enhanced dose rates. As will be shown, events that do not produce the largest peak dose rates can sometimes produce significantly larger total accumulated doses over time if the events are longer in duration. The results presented in this section do not include geomagnetic cutoff effects, and are therefore only valid very near the polar regions. Comparisons with geomagnetic cutoffs included will be presented in Chapter IV below.

The solar proton events of 14 July 2000 and 20 January 2005 exhibit several characteristic differences in their respective proton spectra. The biggest difference can be seen in the spectral hardness of the 20 January event. The spectrum during the peak dose rate (0655 UT) had a very shallow slope, indicating an extremely hard flux (see Figure 30). This turns out to be quite a rare phenomenon in that no other event analyzed or studied had a spectral hardness even close to that of the January event. Though this event showed the greatest softening of the proton spectrum by 10 minutes after the peak dose rate, the spectral hardness and the associated dose rate were still far greater than what was calculated for the 14 July 2000 event (by an order of magnitude). It is interesting to note that the >10 MeV particle flux for the 14 July event at its peak dose rate was over 900

particles/cm^2/sec/str (115%) larger than the >10 MeV particle flux for the 20 January

event during its respective peak dose rate. This demonstrates that the size of the flux is

not as important as the spectral hardness of the flux.

Tables 9 and 10 below show the flux for each event broken out by selected times,

detector channels (P4 – P11), and the total (>10 MeV) flux which is the sum of all the

detector channels. Several times were chosen near the peak dose rates to capture greater

resolution of the event while at its peak. The later times are 2 and 4 hours after the dose

rate peak to show how the event has changed over a longer period of time. For reference,

the estimated dose rates in μSv/hr for each time are listed at the bottom of the tables. A

quick comparison of the January and July events makes clear that the >10 MeV particle

flux alone is insufficient to determine whether an event will produce a large dose rate.

Table 9: Particle fluxes during the 14 July 2000 solar proton event. Fluxes for each detector channel (P4 – P11) are listed, along with the total flux (sum of P4 – P11). The dose rate calculated at 80,000 ft (in μSv/hr) is listed for each time as well. Geomagnetic cutoff effects are not included.

	14 July 2000 (units: particles/cm^2/sec/str)				
Flux	**1200 UT***	**1205 UT**	**1210 UT**	**1400 UT**	**1600 UT**
P4	938.6501	1069.237	1090.3	2764.643	4608.158
P5	531.3683	531.2695	522.3114	631.7894	737.7015
P6	190.9175	185.6522	180.1342	132.851	128.4693
P7	23.0488	22.5454	21.4383	13.9628	11.361
P10	1.2547	1.2325	1.1487	0.5409	0.4129
P11	3.6792	3.4223	3.3372	1.5183	1.2129
Total	1688.919	1813.359	1818.670	3545.305	5487.315
Dose Rate*	33.23	33.01	32.10	22.97	20.21

* Indicates the time when the peak dose rate occurred.
** Dose rates listed for an altitude of 80,000 ft with units of μSv/hr.

Table 10: Particle fluxes during the 20 January 2005 solar proton event. Fluxes for each sensor channel (P4 – P11) are listed, along with the total flux (sum of P4 – P11). The dose rate calculated at 80,000 ft (in µSv/hr) is listed for each time as well. Geomagnetic cutoff effects are not included.

	20 January 2005 (units: particles/cm^2/sec/str)				
Flux	**0655 UT**[*]	**0700 UT**	**0705 UT**	**0855 UT**	**1055 UT**
P4	205.6761	454.2133	753.3003	1265.758	1528.02
P5	161.799	523.1528	862.8429	451.6319	252.6756
P6	135.7994	321.199	400.2872	100.8772	51.2391
P7	82.0098	27.7166	69.8582	6.8252	4.0691
P10	30.9028	7.9909	10.884	1.7701	0.7465
P11	163.6637	30.9294	40.5498	7.1903	3.0406
Total	779.8508	1365.202	2137.722	1834.053	1839.791
Dose Rate[**]	184.02	74.50	105.09	20.79	10.59

[*] Indicates the time when the peak dose rate occurred.
[**] Dose rates listed for an altitude of 80,000 ft with units of µSv/hr.

A better indicator of whether an event will produce a significant dose rate is the amount of flux in the high rigidity detector channels. Figure 35 shows a plot of the sum of the fluxes from channels P7 – P11, which covers rigidities greater than 950 MV (397 MeV). This figure provides a much better explanation for the size of the dose rates, with the January >950 MV proton flux an order of magnitude larger than the other two events for the first half hour. The figure also shows that the July event had a more sustained flux from protons with rigidity >950 MV through 4 hours. This explains why the July dose rates remained high for so long (the dose rate after 4 hours for the July event was nearly 10 µSv/hr larger than the dose rate for the January event after 4 hours) and suggests that smaller yet sustained event can result in a larger total accrued dose during lengthy operations at high altitudes.
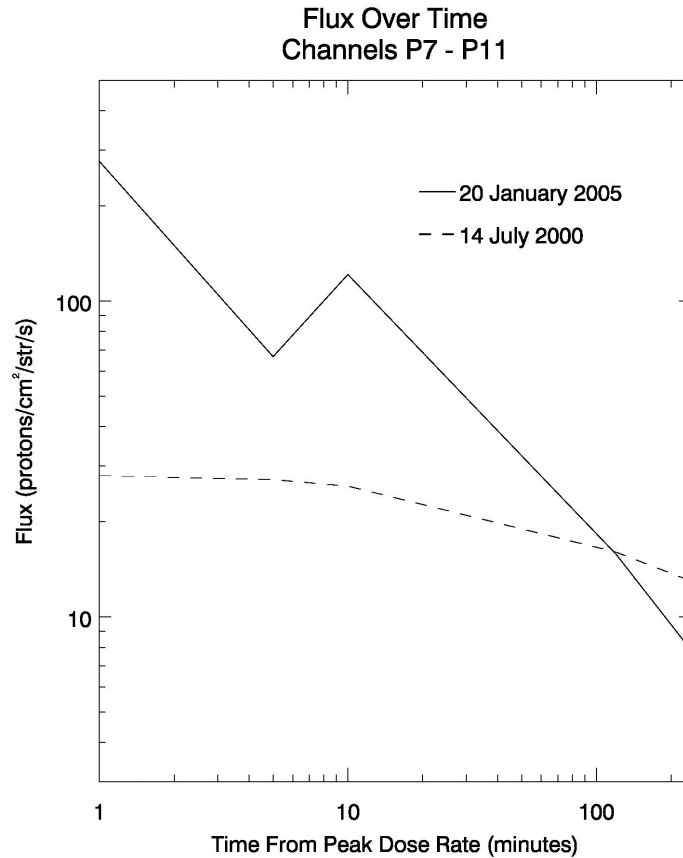
Figure 35: The >950 MV flux over time (on a log/log scale) for the 14 July 2000 and 20 January 2005 solar proton events. Data plotted is from Tables 9 and 10 above.

Table 11 below shows a comparison of the total effective doses accrued during each event for a hypothetical flight at 80,000 ft. Total exposure times calculated were 1, 3, 5, and 10 hours. Radiation doses accrued were measured in μSv. As was shown previously (inTable 10), the dose rates for the January event during the first 10 minutes were an order of magnitude larger than the July event. However, the total 1 hour dose for the January event shown in Table 11 below, while still larger than the dose accrued for the July event, is not as significantly larger as the initial dose rates were. This is because the January event, although powerful at first, decreased rapidly in the flux of particles

86

with rigidities greater than 950 MV. This, combined with the lower event fluence (as

compared to the July event), resulted in the July event causing nearly the same total dose

by the 10 hour point than the January event.

Table 11: Comparison of the total effective dose (in μSv) accrued at 80,000 ft for the indicated time periods during the 14 July 2000 and 20 January 2005 solar proton events. Geomagnetic cutoff effects are not included.

Comparison of Total Effective Doses Accrued During Each Solar Proton Event[*]				
Date	**1 hour**	**3 hours**	**5 hours**	**10 hours**
14 Jul 2000	30.0 μSv	76.5 μSv	116.0 μSv	180.8 μSv
20 Jan 2005	76.5 μSv	128.3 μSv	153.3 μSv	181.4 μSv

[*] Doses calculated for an altitude of 80,000 ft.

Comparisons to Results With Geomagnetic Cutoff

Up until now, results have shown dose rates without taking geomagnetic cutoff

effects into account. However, as was shown in Chapter III: Geomagnetic Cutoff

Determination, the geomagnetic cutoff can significantly affect the rigidity range of

particles that contribute to the radiation environment at aircraft altitudes. Since the dose

rates produced are dependent on the rigidity range of the flux, the geomagnetic cutoff

may be an important factor in determining the amount of radiation received at a particular

location.

The first comparison to be made is be between different levels of geomagnetic

activity. If active geomagnetic conditions, which are characterized by high Kp indices,

cause cutoffs that lead to significantly different dose rates than quiet geomagnetic conditions, which are characterized by low Kp indices, then the level of geomagnetic activity must be taken into account. To perform this comparison, geomagnetic cutoffs were computed during the 20 January 2005 solar proton event at the peak dose rate and 4 hours later.

The dose rates at the event peak (0655 UT) are shown in Figure 36. The ovals nearest the north pole show where the 170 µSv/hr dose rate is, while the equatorward ovals show where the 15 µSv/hr dose rate it. The thick ovals indicate quiet geomagnetic activity levels (Kp=0) while the thin ovals indicate stormy geomagnetic activity levels (Kp=6). This figure makes it clear that geomagnetic activity is more important closer to the geomagnetic pole, and less important closer to the geomagnetic equator. This is to be expected since Figures 26 and 24 indicate that a change in geomagnetic activity will not significantly alter the cutoff for a particle with energies over 5000 MV (4150 MeV), with a cutoff located in the middle latitudes. Changes in geomagnetic activity do, however, affect particles with energies near 500 MV (125 MeV), and with cutoffs located in the high latitudes.

The next comparison to be made is between dose rates calculated without taking geomagnetic cutoff effects into account, and those calculated including these cutoff effects. Dose rates with geomagnetic cutoff effects included were calculated for two locations: one location to represent the mid-latitudes (35° North, 280° East), and one location to represent the high-latitudes (50° North, 280° East). Dose rates calculated without cutoff effects are only valid at the poles.

Dose Rate Dependence on Geomagnetic Activity
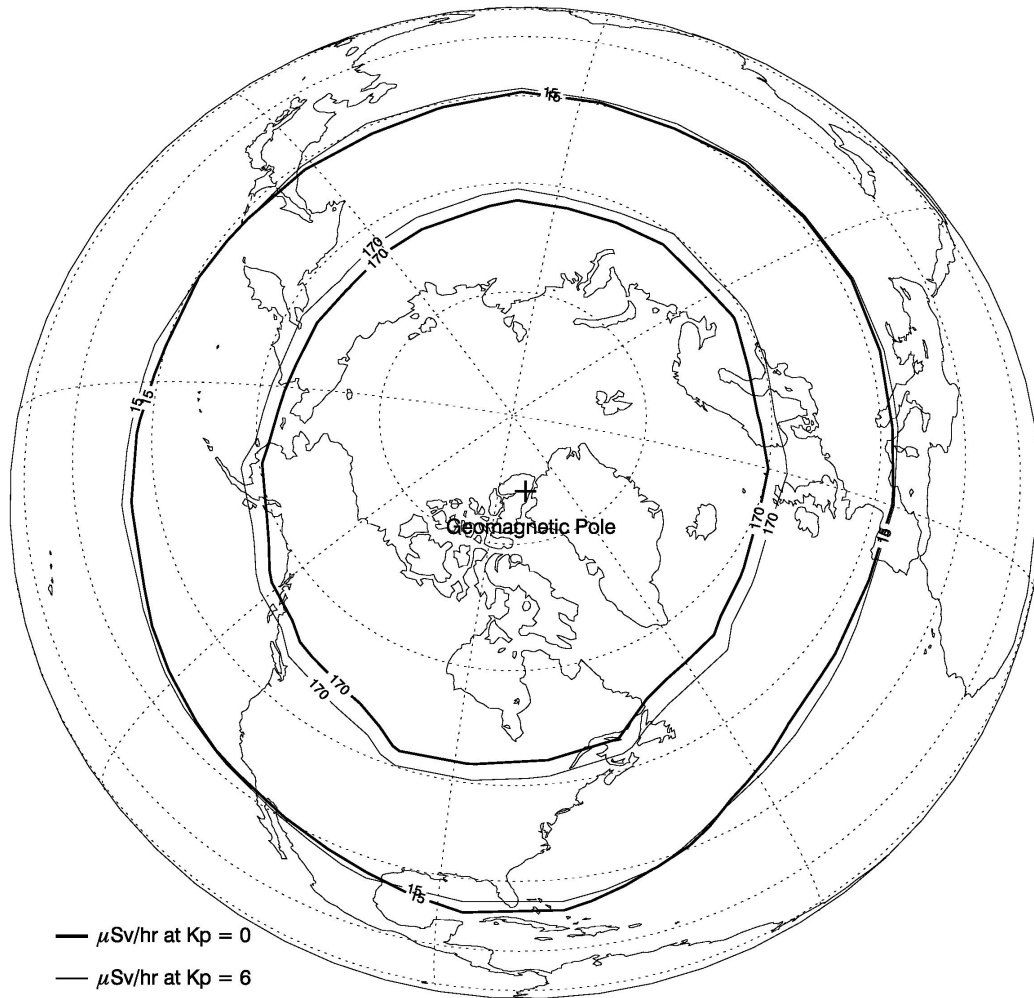
Figure 36: Dose rates in μSv/hr at 0655 UT on 20 January 2005. The thick ovals indicate quiet geomagnetic activity levels (Kp=0); the thin ovals indicate stormy geomagnetic activity levels (Kp=6). The dose rate without taking geomagnetic cutoff effects into account is 184 μSv/hr.

The 20 January and 14 July events were chosen for comparison because of the large initial dose rate in the January event and long duration of the solar proton event in the July case. Calculations were made with no geomagnetic cutoff taken into account, and with cutoffs computed at two levels of geomagnetic activity (characterized by Kp=0 and Kp=6). This comparison, shown in Tables 12 and 13 below, will therefore show the

dependence of the total accrued dose on the level of geomagnetic activity as well as the

dependence on latitude. All calculations shown below are for an altitude of 80,000 ft.

Table 12: Comparison of the geomagnetic cutoff dependency of the total doses accrued during the 14 July 2000 solar proton event at 80,000 ft. Geomagnetic cutoffs and doses were calculated for two locations representing the middle and high latitudes.

Geomagnetic Cutoff Dependency 14 July 2000					
Location	Geomagnetic Cutoff	1 hour	3 hours	5 hours	10 hours
Middle Latitudes: 35N/280E	No Cutoff	30.0 μSv	76.5 μSv	116.0 μSv	180.8 μSv
	3071 MV (Kp=0)	0.1 μSv	0.2 μSv	0.4 μSv	0.7 μSv
	2558 MV (Kp=6)	0.2 μSv	0.5 μSv	0.8 μSv	1.3 μSv
High Latitudes: 50N/280E	No Cutoff	30.0 μSv	76.5 μSv	116.0 μSv	180.8 μSv
	344 MV (Kp=0)	29.5 μSv	74.2 μSv	110.7 μSv	164.8 μSv
	224 MV (Kp=6)	30.0 μSv	76.3 μSv	115.6 μSv	178.8 μSv

Table 13: Comparison of the geomagnetic cutoff dependency of the total doses accrued during the 20 January 2005 solar proton event at 80,000 ft. Geomagnetic cutoffs and doses were calculated for two locations representing the middle and high latitudes.

Geomagnetic Cutoff Dependency 20 January 2005					
Location	Geomagnetic Cutoff	1 hour	3 hours	5 hours	10 hours
Middle Latitudes: 35N/280E	No Cutoff	76.5 μSv	128.3 μSv	153.3 μSv	181.4 μSv
	3071 MV (Kp=0)	5.2 μSv	7.1 μSv	8.0 μSv	9.4 μSv
	2558 MV (Kp=6)	7.2 μSv	10.0 μSv	11.3 μSv	13.2 μSv
High Latitudes: 50N/280E	No Cutoff	76.5 μSv	128.3 μSv	153.3 μSv	181.4 μSv
	344 MV (Kp=0)	76.2 μSv	126.9 μSv	151.0 μSv	178.0 μSv
	224 MV (Kp=6)	76.5 μSv	128.3 μSv	153.3 μSv	181.4 μSv

Cutoff effects can drastically reduce the accrued doses, especially in the middle latitudes, where doses can be reduced by nearly an order of magnitude. At higher latitudes, total accrued doses are much higher because the cutoffs at these locations are so low. Along the 280°E meridian, the cutoff effects drastically reduce the dose rates equatorward of approximately 45°. This is about 35° equatorward of the geomagnetic pole, which is currently located at approximately 80°N, 288°E in the northern hemisphere. In the transition zone, where dose rates begin to shrink rapidly due to geomagnetic cutoff effects, accounting for the level of geomagnetic activity is especially important. A change in geomagnetic conditions from quiet to stormy can cause a shift in cutoffs by up to 15°, which may lead to a drastic increase in the dose rates expected.

Comparisons to CARI-6 Output

It is important to compare the results of this study with output produced by the CARI-6 model which is currently used to estimate dose rates at aviation altitudes. As mentioned previously in Chapter II: The CARI-6 Radiation Dose Predictive Code, this model only accounts for galactic cosmic rays (5). It does however take into account geomagnetic cutoffs and it also uses an average heliocentric potential to account for some changes in geomagnetic activity. To make the comparisons shown below, the maximum dose rates were used, thus assuming a location very near the geomagnetic poles such that there is no cutoff. Further, all results listed below were calculated for an altitude of 60,000 ft because this is the maximum altitude available in the CARI-6 model (5).

Table 14 below shows the 1, 3, 5, and 10 hour total accrued doses in µSv for the 20 January 2005 and the 14 July 2000 events. Doses computed by the CARI-6 program

are the result of galactic cosmic rays, while doses due to solar protons have the galactic cosmic ray flux subtracted from the total flux. The total dose received is the sum of the galactic and solar particles and is listed as the Total Dose.

The January event shows that a significant portion of the total dose during the first 3 hours came from solar protons. After 5 hours, the flux of energetic protons from the sun had decreased appreciably, and the total dose accrued began to level off. However, even at 10 hours after the event peak, a significant portion of the total dose (over 38%) was due to solar protons.

The July solar proton event initially contributed a smaller percentage to the total accrued dose than the January event. Total accrued doses from solar protons after 1 and 3 hours were nearly equivalent to the doses accrued from galactic cosmic rays. However, since the July event was characterized by a longer sustained flux of solar protons of high rigidity, the dose from solar protons 10 hours after the event peak was still over 46% of the total accrued dose.

The table below shows that up to 10 hours after a large solar proton event, doses due to solar protons can still cause a substantial percentage of the radiation dose encountered at aviation altitudes. After 10 hours, the dose rate during the January event dropped below 10% of the total dose rate, and therefore, the contribution of solar protons to the total accrued doses decreased rapidly. Dose rates due to solar protons in the July event were still nearly 25% of the total dose rate even after the 12 hour point, indicating again that this event was unique in its duration.

Table 14: Accrued doses in µSv at 60,000 ft for the 20 January 2005 and 14 July 2000 solar proton events. Accrued doses are from galactic cosmic rays alone, solar protons alone, and galactic + solar particles. Doses due to galactic cosmic rays were computed using the CARI-6 model (5).

Total Accrued Doses 20 January 2005				
Particle Origin	1 hour	3 hours	5 hours	10 hours
Galactic	14.3 µSv	42.9 µSv	71.5 µSv	143.0 µSv
Solar	41.23 µSv	65.32 µSv	76.47 µSv	88.63 µSv
Total Dose (galactic + solar)	55.53 µSv	108.22 µSv	147.97 µSv	231.63 µSv
Total Accrued Doses 14 July 2000				
Particle Origin	1 hour	3 hours	5 hours	10 hours
Galactic	11.2 µSv	33.6 µSv	56.0 µSv	112.0 µSv
Solar	11.24 µSv	28.23 µSv	42.61 µSv	66.17 µSv
Total Dose (galactic + solar)	22.44 µSv	61.83 µSv	98.61 µSv	178.17 µSv

Comparisons to Measured Data

Ideally, the dose rates predicted by this study for the 14 July 2000 and 20 January 2005 solar proton events would be compared to actual measurements made by aircraft in flight at 80,000 ft during the events. Unfortunately, the rarity of large solar proton events, and the lack of radiation monitors onboard aircraft mean that actual measurements of radiation doses during solar proton events are extremely rare. In fact, no measurements were found for aircraft flying during any of the significant solar proton events for which accurate particle flux data is available.

Data was found, however, during two large solar proton events that occurred on 29 September 1989 and 24 October 1989, during which a Concorde jet equipped with a

dosimeter was flying at an altitude of 57,000 ft. Peak dose rates measured during the two events by the Concorde were 61 and 53 µSv/hr respectively. It is important to note that the Concorde flight in September of 1989 was not at the peak of the solar proton event (4:91). If these numbers are extrapolated out to 1 hour, they give a total accrued dose of 61 µSv and 53 µSv respectively for the two flights. These numbers show good correspondence to the doses presented in Table 14 for the 20 January 2005 solar proton event, where a 1 hour accumulated radiation dose due to solar and galactic particles was calculated to be 55.53 µSv.

A direct comparison between the calculated dose rates presented in this study and actual dose rate measurements during the same event would be ideal. However, no direct dose rate measurements were found for aircraft airborne during large solar proton events for which reliable solar proton flux information from the GOES Space Environment Monitor was available. Although there are no measurements available for direct comparisons, the results from the Concorde flight in 1989 suggest that the numbers presented in this study are within an order of magnitude of the actual doses produced at high altitudes during a solar proton event.

V. Summary, Conclusions, and Recommendations

Summary

Solar proton events often cause a significant enhancement to the radiation environment at aircraft altitudes. Determining the effective dose rate that personnel and equipment are subject to during one of these events is accomplished by measuring the flux of solar protons in the near-earth environment, using this to model the spectrum of the particles in rigidity, and then using currently established conversion coefficients to convert the modeled spectrum into a dose rate.

The measurement of solar protons is accomplished by a suite of sensors called the Space Environment Monitor onboard the NOAA GOES-series spacecraft. This data is available in real-time from the NOAA SEC. A procedure has been outlined, first developed by *Copeland et al.* (1), to convert the energetic particle data from the SEC into effective dose rates at a range of altitudes from the surface of the earth, up to 80,000 ft above mean sea level.

The process was then combined with a method to compute geomagnetic cutoff rigidities for different levels of geomagnetic activity. This further refines the effective dose rate calculation to only include those solar protons that are energetic enough to penetrate the earth's magnetosphere and arrive at a given location.

Two large solar proton events (14 July 2000 and 20 January 2005) were then investigated to determine relationships between event fluence, spectral hardness, and effective dose rate.

Conclusions

Based on the examination of the three solar proton events in Chapter IV, several conclusions can be drawn with respect to solar proton events, their interaction with the earth's magnetic field, and the subsequent radiation that may be produced in the earth's atmosphere.

The first conclusion is that the effect of spectral hardness is of greater importance to the amount of radiation dose received at aircraft altitude than the >10 MeV flux. An accurate model of the solar proton spectrum is extremely important in determining the spectral hardness, and thus for predicting dose rates due to solar proton events. Three methods were presented for modeling solar proton spectra, however all three showed deficiencies in that the spectra contained discontinuities and the spectra were extrapolated at rigidities higher than 1343 MV. The results presented in Chapter IV demonstrated that the size of the >10 MeV solar proton flux is not as important as the energy distribution of the protons within the flux. The 20 January 2005 event was much lower in total flux than the 14 July 2000 event. However, because the 20 January 2005 event was characterized by such a high spectral hardness during the first half hour, dose rates were an order of magnitude larger than the July event. This is because the bulk of the dose rate comes from the higher rigidities.

Another factor in the cause of large radiation doses is the duration of the solar proton event. An event such as the 20 January 2005 event that produced extremely high dose rates, but only lasted a few hours may not produce a total accrued dose as large as a smaller event that lasts for many hours. The 14 July 2000 event was characterized by

much smaller dose rates initially than the 20 January 2005 event. However, the dose rates during the July event did not fall off over time as quickly as the January event. While not as large of a threat for the first few hours, the July event produced equally large total accrued doses after 5 hours of continuous exposure. Thus, the duration of the energetic particle flux is also an important factor that must be considered when forecasting radiation doses at high altitudes. Simply avoiding high altitude operations for the first 2 to 3 hours after a solar proton event may not always be an adequate solution.

The varying nature of solar proton events makes the challenge of forecasting dose rates prior to an event onset a challenging one. Since dose rates are not only dependent on the flux of energetic particles, but also on the spectral hardness and the duration of the event, providing real-time warnings is the most effective way to deal with the problem at the current time. The differing nature of the solar proton events studied in Chapter IV suggests that there may be different mechanisms which accelerate the protons in these events. If this is the case, then understanding these mechanisms may also explain why the spectral hardness and duration of the events can differ so much. All of these concepts must be understood before a reliable method for forecasting radiation dose rates due to solar proton events can be developed.

The next conclusion to be drawn is that magnitude of the dose rate is dependent on the location of the particle flux within the spectrum of rigidities. Both events studied showed that the bulk of the dose rate came from the rigidity range from 400 to 2000 MV, which corresponds to approximately 82 to 1270 MeV (the only exception was the first half hour of the 20 January 2005 event). This rigidity range corresponds to approximate

geomagnetic cutoff latitudes of between 45° and 55°. For the initial stages of the 20 January 2005 event, cutoff latitudes were decreased to below 40° in some locations. Further, the 400 to 2000 MV rigidity range is within the region that is affected by geomagnetic activity, and therefore the level of activity must be taken into account when computing geomagnetic cutoffs. The effect of the geomagnetic cutoffs cannot typically be ignored, unless flights are conducted exclusively over the polar regions (at latitudes greater than approximately 75°). Outside of these regions, the geomagnetic cutoff will have a significant effect on the radiation dose rates encountered.

Comparisons to CARI-6 output made in Chapter IV showed that the dose rates resulting from solar protons during large solar proton events were equivalent if not greater than dose rates produced by galactic cosmic rays. This means that using the CARI-6 program alone to predict dose rates may not provide accurate data for a period of time after the eruption of a large solar flare or CME. Thus work must continue to understand the nature of solar proton events so that improved methods for modeling their spectra and predicting dose rates can be developed.

Finally, although no dose rates were actually measured by dosimeters onboard aircraft during the solar proton events presented, limited data is available from dosimeters onboard the Concorde aircraft which was airborne at 57,000 ft during the large solar proton event of 29 September 1989. During this flight, a peak dose rate of 61 µSv/hr was measured, which can be extrapolated to a 1 hour accumulated dose of 61 µSv. This value corresponds well to the 1 hour accumulated dose predicted during the 20 January 2005 solar proton event. This gives credibility to the dose rate calculations made in this paper.

The main thrust of this study is the determination of whether solar proton events produce radiation doses large enough to endanger personnel flying at high altitudes. Based on the information gathered from the two recent solar proton events studied, including the largest GLE in the last 50 years, the radiation dose rates are significant enough to be concerned about, but do not appear to be so large that encountering a single event will cause life-altering effects.

The FAA recommended limit for radiation exposure is 20 mSv per year averaged over a 5 year period (see Chapter I). For aircraft flying at 80,000 ft during solar minimum (so that the galactic cosmic ray flux is maximized), and at high latitudes where geomagnetic cutoffs are small, the average dose rate received from the background galactic cosmic radiation is approximately 15 µSv/hr. A total annual dose will of course depend on the amount of time spent flying at these high altitudes and latitudes. Assuming an annual flight time of 1,200 hours, all flown at 80,000 ft and over the geomagnetic pole, a pilot could expect to receive an annual dose of 18 mSv.

Adding the additional dose accrued due to solar protons may exceed the recommended limit of 20 mSv/yr. Assuming a 20-hour flight at 80,000 ft over the geomagnetic pole, the total dose received during a large solar proton event could conceivably reach 500 µSv, or .5 mSv (see Tables 11 and 14). Although this number is small in comparison to the recommended annual dose limit, flying through several large solar proton events would quickly cause a pilot to receive more than 5% of the annual limit. Therefore, it is necessary to actively monitor the dose rates produced by ongoing solar proton events so accurate radiation exposure amounts can be kept in crews' records.

Additionally, flights can be diverted around altitudes or latitudes where the risk due to radiation exposure is deemed too high.

The conclusions made in this section are all based on the assumptions discussed in Chapter III. Knowing how these assumptions affect the outcome and improving measurement and modeling techniques are important to improving the radiation dose rate estimates. Several topics for further research in these areas are suggested next.

Recommendations for Future Work

The problem of determining radiation dose rates at high altitudes due to solar energetic particles is by no means solved. A key assumption which requires further investigation is how much the energetic particle measurements vary at geosynchronous orbit due to anisotropies in the solar proton flux. The method used to model the solar proton spectrum needs more examination as well. Specifically, there is a need to develop a method to approximate the solar proton spectrum in a more continuous manner. Instrumentation to measure energetic particles in specific energy bins above 700 MeV would provide greater confidence in the solar proton spectrum above 700 MeV.

As research continues on radiation doses and shielding techniques, the method of converting the modeled solar proton spectra into effective dose rates will undergo changes as well. The MCNPX calculations are being continuously improved, and using anisotropic particle fluxes at 100 km would better simulate the actual flux of energetic particles incident at the top of the earth's atmosphere during a solar proton event.

Another area for further study is measuring the shielding effect of the airframe and any techniques or materials used to provide additional shielding to aircrew.

Finally, the ability to actually forecast radiation dose rates before a solar proton event occurs is possibly the biggest challenge. This will require further work to determine why certain solar proton events produce such hard fluxes while others do not.

Appendix A: Selected Rigidity to Energy Conversions (27:112)

PROTON Rigidity (MV)	Energy (MeV)	PROTON Rigidity (MV)	Energy (MeV)	PROTON Rigidity (MV)	Energy (MeV)	PROTON Rigidity (MV)	Energy (MeV)
1.0	0.001	71.0	2.681	510.0	129.594	3200.0	2396.122
2.0	0.002	72.0	2.757	520.0	134.403	3300.0	2492.194
3.0	0.005	73.0	2.834	530.0	139.285	3400.0	2588.484
4.0	0.009	74.0	2.912	550.0	149.257	3500.0	2684.975
5.0	0.013	75.0	2.991	560.0	154.346	3600.0	2781.652
6.0	0.019	76.0	3.071	570.0	159.503	3700.0	2878.500
7.0	0.026	77.0	3.153	580.0	164.726	3800.0	2975.506
8.0	0.034	78.0	3.235	590.0	170.015	3900.0	3072.659
9.0	0.043	79.0	3.318	600.0	175.369	4000.0	3169.949
10.0	0.053	80.0	3.403	610.0	180.786	4100.0	3267.366
11.0	0.064	81.0	3.488	620.0	186.266	4200.0	3364.902
12.0	0.077	82.0	3.575	630.0	191.808	4300.0	3462.548
13.0	0.090	83.0	3.662	640.0	197.411	4400.0	3560.297
14.0	0.104	84.0	3.751	650.0	203.074	4500.0	3658.144
15.0	0.120	85.0	3.840	660.0	208.796	4600.0	3756.081
16.0	0.136	86.0	3.931	670.0	214.577	4700.0	3854.103
17.0	0.154	87.0	4.023	680.0	220.415	4800.0	3952.206
18.0	0.173	88.0	4.116	690.0	226.309	4900.0	4050.383
19.0	0.192	89.0	4.210	700.0	232.259	5000.0	4148.632
20.0	0.213	90.0	4.304	710.0	238.265	5100.0	4246.948
21.0	0.235	91.0	4.400	720.0	244.324	5200.0	4345.327
22.0	0.258	92.0	4.497	730.0	250.436	5300.0	4443.765
23.0	0.282	93.0	4.596	740.0	256.601	5400.0	4542.261
24.0	0.307	94.0	4.695	750.0	262.818	5500.0	4640.809
25.0	0.333	95.0	4.795	760.0	269.085	5600.0	4739.409
26.0	0.360	96.0	4.896	770.0	275.402	5700.0	4838.056
27.0	0.388	97.0	4.998	780.0	281.769	5800.0	4936.750
28.0	0.417	98.0	5.102	790.0	288.184	5900.0	5035.486
29.0	0.448	99.0	5.206	800.0	294.646	6000.0	5134.265
30.0	0.479	100.0	5.311	810.0	301.156	6100.0	5233.082
31.0	0.512	110.0	6.423	820.0	307.712	6200.0	5331.937
32.0	0.545	120.0	7.639	830.0	314.313	6300.0	5430.828
33.0	0.580	130.0	8.959	840.0	320.959	6400.0	5529.753
34.0	0.616	140.0	10.382	850.0	327.650	6500.0	5628.710
35.0	0.652	150.0	11.909	860.0	334.383	6600.0	5727.698
36.0	0.690	160.0	13.538	870.0	341.160	6700.0	5826.717
37.0	0.729	170.0	15.269	880.0	347.978	6800.0	5925.763
38.0	0.769	180.0	17.102	890.0	354.838	6900.0	6024.837
39.0	0.810	190.0	19.035	900.0	361.738	7000.0	6123.938
40.0	0.852	200.0	21.069	910.0	368.679	7100.0	6223.063
41.0	0.895	210.0	23.203	920.0	375.659	7200.0	6322.212
42.0	0.939	220.0	25.435	930.0	382.677	7300.0	6421.384
43.0	0.984	230.0	27.766	940.0	389.734	7400.0	6520.578
44.0	1.031	240.0	30.194	950.0	396.829	7500.0	6619.793
45.0	1.078	250.0	32.720	960.0	403.961	7600.0	6719.029
46.0	1.126	260.0	35.341	970.0	411.128	7700.0	6818.285
47.0	1.176	270.0	38.058	980.0	418.332	7800.0	6917.559
48.0	1.226	280.0	40.869	990.0	425.571	7900.0	7016.852
49.0	1.278	290.0	43.774	1000.0	432.845	8000.0	7116.162
50.0	1.331	300.0	46.772	1100.0	507.375	8100.0	7215.489
51.0	1.384	310.0	49.862	1200.0	584.825	8200.0	7314.832
52.0	1.439	320.0	53.043	1300.0	664.773	8300.0	7414.191
53.0	1.495	330.0	56.315	1400.0	746.862	8400.0	7513.565
54.0	1.552	340.0	59.676	1500.0	830.796	8500.0	7612.953
55.0	1.610	350.0	63.126	1600.0	916.323	8600.0	7712.356
56.0	1.669	360.0	66.663	1700.0	1003.234	8700.0	7811.772
57.0	1.729	370.0	70.287	1800.0	1091.350	8800.0	7911.202
58.0	1.790	380.0	73.996	1900.0	1180.521	8900.0	8010.644
59.0	1.852	390.0	77.791	2000.0	1270.620	9000.0	8110.098
60.0	1.916	400.0	81.669	2100.0	1361.537	9100.0	8209.565
61.0	1.980	410.0	85.631	2200.0	1453.179	9200.0	8309.042
62.0	2.045	420.0	89.674	2300.0	1545.466	9300.0	8408.531
63.0	2.112	430.0	93.798	2400.0	1638.328	9400.0	8508.031
64.0	2.179	440.0	98.003	2500.0	1731.706	9500.0	8607.541
65.0	2.248	450.0	102.286	2600.0	1825.548	9600.0	8707.062
66.0	2.317	460.0	106.648	2700.0	1919.807	9700.0	8806.592
67.0	2.388	470.0	111.087	2800.0	2014.443	9800.0	8906.132
68.0	2.460	480.0	115.602	2900.0	2109.423	9900.0	9005.680
69.0	2.532	490.0	120.192	3000.0	2204.713	10000.0	9105.238
70.0	2.606	500.0	124.856	3100.0	2300.288		

Appendix B: Derivation of Solar Proton Spectra Using An Alternate Method (25)

In calculating the dose rate due to solar energetic particles, the energy spectrum of the incoming particles must first be modeled. The following derivation provides an alternative method for use in modeling the solar proton spectrum. This method makes use of the I3, I4, I5, and I7 integral particle fluxes, as well as the P8, P9, P10, and P11 HEPAD particle fluxes as reported by the SEC. For information about these fluxes, see Chapter III: An Alternate Method for Modeling the Solar Proton Spectrum.

Before beginning, the HEPAD particle fluxes reported by the SEC are converted to the original instrument count rates, and the background galactic cosmic ray count rate is subtracted. This process is described in Chapter III: An Alternate Method for Modeling the Solar Proton Spectrum. To convert the solar proton count rates to integral fluxes, with units of protons/cm^2/sec/str, each HEPAD channel is divided by the instrument's geometric factor (0.73 cm^2·str) (24:6). Finally, for the HEPAD channels (P8, P9, P10, and P11) to truly represent integral fluxes, the flux of the larger channels is added to the smaller ones in the following manner:

$$
\begin{aligned}
J(E > 700 \text{ MeV}) &= J^{*}{}_{P11} \\
J(E > 510 \text{ MeV}) &= J^{*}{}_{P10} + J^{*}{}_{P11} \\
J(E > 420 \text{ MeV}) &= J^{*}{}_{P9} + J^{*}{}_{P10} + J^{*}{}_{P11} \\
J(E > 330 \text{ MeV}) &= J^{*}{}_{P8} + J^{*}{}_{P9} + J^{*}{}_{P10} + J^{*}{}_{P11}
\end{aligned}
\tag{20}
$$

which results in the following set of eight integral fluxes (25):

$$J > 10 MeV \qquad J > 330 MeV$$
$$J > 30 MeV \qquad J > 420 MeV$$
$$J > 50 MeV \qquad J > 510 MeV$$
$$J > 100 MeV \qquad J > 700 MeV$$

Just as in the original method, each of the eight integral flux channels can be fit with a power law of the form

$$J\left(E_n\right) = \int_{E_n}^{\infty} f_0 E^{-\gamma} dE$$
$$= \frac{f_0}{\gamma - 1} E_n^{-\gamma+1} \qquad (21)$$

Making a few substitutions, the following expression for each integral flux is derived:

$$J_n = J_0^n E_n^{-\beta}, \qquad (22)$$

where the spectral hardness, β, and the intensity, J_0, are defined as

$$\beta = \gamma - 1$$
$$J_0 = \frac{f_0}{\gamma - 1} \qquad (23)$$

(Note that this requires that $\gamma \neq 1$ otherwise $J \to \infty$.) (25)

Given Eq. (22), the integral channels can be fit with power laws of the form

$$J(E > 10 \text{ MeV}): J_{10} = J_0^{10}(E = 10 \text{ MeV})^{-\beta_{10}}, \qquad (24)$$

to create a piece-wise continuous approximation of the solar proton spectrum. Solving for the constants J_0^{10} and β_{10}, we find that in general,

$$\beta_n = \frac{\log\left(\dfrac{J_{n+1}}{J_n}\right)}{\log\left(\dfrac{E_n}{E_{n+1}}\right)}.$$

(25)

$$J_0^n = J_n E_n^{\beta_n}$$

This allows a piecewise spectrum to be fit over all of the integral channels up to the last one $\left(J > 700 MeV\right)$. For the last integral channel, the constants J_0^{700} and β_{700} are obtained using the following relations:

$$\beta_{700} = \frac{\log\left(\dfrac{J_{700}}{J_{330}}\right)}{\log\left(\dfrac{E_{330}}{E_{700}}\right)}.$$

(26)

$$J_0^{700} = J_{700} E_{700}^{\beta_{700}}$$

These relations look backward several channels, which enables the last integral channel to be fit to the power law (25).

This process creates eight solar proton spectra, which can be combined to form a piecewise-continuous approximation of the entire solar proton spectrum for rigidities greater than 137 MV (10 MeV). This spectrum is then used to estimate the dose rates at specified altitudes and locations using the process described in Chapter III: Effective Dose Calculation.

Bibliography

1. Copeland, K., *et al.* "Solar Radiation Alert System," Department of Transportation, Federal Aviation Administration, Office of Aerospace Medicine, DOT/FAA/AM-05/14, Washington DC, 2005

2. Cosmic Ray Station of the University of Oulu. "Cosmic Ray Database," University of Oulu, Finland. http://cosmicrays.oulu.fi. 15 Nov 2005.

3. Duldig, M. "GLE List." http://neutronm.bartol.udel.edu/~pyle/GLE_List.txt. 12 Apr 2005.

4. Dyer, C.S., *et al.* "Calculations and Observations of Solar Particle Enhancements to the Radiation Environment at Aircraft Altitudes," *Advances in Space Research*. Vol. 32, No. 1, 81-93, 2003.

5. Federal Aviation Administration, Civil Aerospace Medical Institute. "Galactic Radiation Received In Flight." http://jag.cami.jccbi.gov./cariprofile.asp. 6 January 2006.

6. Freeman, J.W., *et al.* "Specifying Geomagnetic Cutoffs for Solar Energetic Particles," *Space Weather*, Geophysical Monograph 125, Geophysical Union, 191-194, 2001.

7. Friedberg, W., *et al.* "What Aircrews Should Know About Their Occupational Exposure to Ionizing Radiation," Office of Aerospace Medicine, Washington, D.C., October 2003.

8. Goddard Space Flight Center, Space Physics Data Facility. "Tsyganenko Magnetospheric Model, 1989." http://modelweb.gsfc.nasa.gov/magnetos/data-based/T89c.html. 10 Nov 2005.

9. Hargreaves, J.K. *The Solar-Terrestrial Environment*. Cambridge University Press, New York, NY, 1992.

10. Houseman, J., *et al.* "Listening For Cosmic Rays! The Inuvik Neutron Monitor," Aurora College. http://neutronm.bartol.udel.edu//listen/main.html. 1996.

11. Mursula, K., *et al.* "The Heliospheric Physics and Cosmic Rays," Lecture Notes, University of Oulu, 2003.

12. National Geophysical Data Center, GOES Space Environment Monitor. "Direct Access to Data & Plots." http://goes.ngdc.noaa.gov/data/plots. 12 Dec 2005.

13. National Geophysical Data Center. "Solar – Terrestrial Physics." http://www.ngdc.noaa.gov/stp/stp.html. 11 Dec 2005.

14. National Oceanic and Atmospheric Administration, National Aeronautics and Space Administration, and United States Air Force. U.S. Standard Atmosphere, 1976. NOAA S/T 76-1562, Washington, DC: U.S. Government Printing Office, 1976.

15. O'Brien, K., *et al.* "The Atmospheric Radiation Response to Solar-Particle-Events," *Advances in Space Research, 32,* 73-80, 2003.

16. O'Brien, K., *et al.* "World-Wide Radiation Dosage Calculations For Air Crew Members," *Advances in Space Research, 31*, 835-840, 2003.

17. Pellicioni, M., "Overview Of The Fluence-To-Effective Dose And Fluence-To-Ambient Dose Equivalent Conversion Coefficients For High Energy Radiation Calculated Using The Fluka Code," *Radiation Protection Dosimetry*, Vol. 88, No. 4, 279-297, 2000.

18. Reames, D.V., "SEPs: Space Weather Hazard in Interplanetary Space," *Space Weather*, Geophysical Monograph 125, Geophysical Union, 101-107, 2001.

19. Reeves, G.D. "6 Magnetic Field Models Compared." http://leadbelly.lanl.gov/reeves/papers/talks/1995_GEM_poster/gem_1995.html. 4 Jan 2006.

20. Reitz, G., "Radiation Environment in the Stratosphere," *Radiation Protection Dosimetry*, Vol. 48, No. 1, 5-20, 1993.

21. Roesler, S., *et al*. "Monte Carlo Calculations of the Radiation Field At Aircraft Altitudes," *Radiation Protection Dosimetry*, Vol. 98, No. 4, 367-388, 2002.

22. Sauer, H. "Notes on the Natural Radiation Hazard at Aircraft Altitudes," CIRES/NOAA. http://www.sec.noaa.gov/info/RadHaz.html. 2000.

23. Sauer, H. "On-line Determination of Geomagnetic Transmission Functions (Cutoffs)," Cooperative Institute for Research in Environmental Sciences (CIRES), NOAA National Geophysical Data Center (NGDC), Feb 2000.

24. Sauer, H. "Report on Project: Analysis of GOES Particle Data and the Development of s Processing Procedure in Support of FAA Requirements for Radiation Exposure Estimation at Aircraft Altitudes," Boulder, CO: CIRES/NOAA-NGDC, 2003.

25. Sauer, H., Private Communication, September 2005

26. Smart, D.F., *et al*. "A Review of Geomagnetic Cutoff Rigidities for Earth-Orbiting Spacecraft," *Advances in Space Research* (2004).

27. Smart, D.F., *et al.* "Final Report – Geomagnetic Cutoff Rigidity Computer Program." http://modelweb.gsfc.nasa.gov/sun/cutoff.html. 2001.

28. Smart, D.A., *et al. Geophysics Handbook*, Chapter 6, "Galactic Cosmic Radiation and Solar Energetic Particles". Publisher, Place, ST, Year.

29. Smart, D.F., *et al*. "The Limitations of Using Vertical Cutoff Rigidities Determined From the IGRF Magnetic Field Models For Computing For Computing Aircraft Radiation Dose," *Advances in Space Research,* 32, 95-102, 2003

30. Smart, D.F., *et al*. "The Local Time Dependence of the Anisotropic Solar Cosmic Ray Flux," *Advances in Space Research,* 32, 109-114, 2003.

31. Space Environment Center. "Glossary of Solar-Terrestrial Terms." http://www.sec.noaa.gov/info/glossary.html. 4 Jan 2006.

32. Space Environment Center. "Space Weather Data and Products." http://www.sec.noaa.gov/ftpdir/warehouse. 21 Oct 2005.

33. Space Environment Center. "Summer 2003 – GOES Designation Changes." http://www.sec.noaa.gov/Data/notices.html#2003GOESchanges. 15 May 2003.

34. Space Environment Information System. "GOES-11 Query Form." http://www.spenvis.oma.be/spenvis/help/models/databases/goes_11.html. 12 Dec 2005.

35. Space Today Online. "The Sun, Views of the 'Bastille Day' Sun, July 2000." http://www.spacetoday.org/SolSys/Sun/BastilleDaySatViews.html. 28 Dec 2005.

36. Sundstrom, J., Private Communication, 11 January 2006.

37. Turner, R. "What We Must Know About Solar Particle Events to Reduce the Risk to Astronauts," *Space Weather*, Geophysical Monograph 125, Geophysical Union, 39-44, 2001.

38. University Partnering for Operational Support (UPOS). "Solar Penetration Into the High-Latitude Ionosphere: Cutoff Latitudes." http://sd-www.jhuapl.edu/UPOS/SPP/index.html. 10 Nov 2005.

39. Ziegler, J.F. "Terrestrial Cosmic Rays," *IBM Journal of Research and Development,* *40,* 19-40, 1996.

REPORT DOCUMENTATION PAGE

1. REPORT DATE *(DD-MM-YYYY)*	2. REPORT TYPE	3. DATES COVERED *(From - To)*
06-03-2006	Master's Thesis	Sep 2004 - Mar 2006

4. TITLE AND SUBTITLE

Prediction of Flight-Level Radiation Hazards Due To Solar Energetic Particles

5a. CONTRACT NUMBER

5b. GRANT NUMBER

5c. PROGRAM ELEMENT NUMBER

6. AUTHOR(S)

Sattler, Matthew, P., Captain, USAF

5d. PROJECT NUMBER

5e. TASK NUMBER

5f. WORK UNIT NUMBER

7. PERFORMING ORGANIZATION NAME(S) AND ADDRESS(ES)
Air Force Institute of Technology
Graduate School of Engineering and Management (AFIT/EN)
2950 Hobson Way
WPAFB OH 45433-7765

8. PERFORMING ORGANIZATION REPORT NUMBER

AFIT/GAP/ENP/06-16

9. SPONSORING/MONITORING AGENCY NAME(S) AND ADDRESS(ES)
AFWA/DN
Attn: Lt Col Trey Cade
106 Peacekeeper Dr
OFFUT NE 68113   DSN: 271-6177

10. SPONSOR/MONITOR'S ACRONYM(S)

11. SPONSOR/MONITOR'S REPORT NUMBER(S)

12. DISTRIBUTION/AVAILABILITY STATEMENT
APPROVED FOR PUBLIC RELEASE; DISTRIBUTION UNLIMITED

13. SUPPLEMENTARY NOTES

14. ABSTRACT
The radiation environment at aircraft altitudes is caused primarily by high-energy particles originating from outside the near-earth environment. These particles generally come from outside our solar system and are called galactic cosmic rays. Occasionally however, a transient solar event will also accelerate energetic protons toward the earth. If these protons reach the upper atmosphere, they produce secondary particles via collisions, resulting in increased radiation levels in the atmosphere. Air crews and electronic systems flying at high altitudes during one of these events are subjected to these increased levels of radiation which can result in health problems for personnel and soft errors in electronics. Much work has been performed to calculate radiation dose rates at flight levels due to non-solar energetic particles, however very few dose rate measurements have been made shortly after the eruption of a large solar flare. Using energetic proton data measured at geosynchronous orbits and Monte Carlo transport codes, an attempt is made to estimate radiation dose rates at different altitudes and locations during solar events. The goal is to provide accurate information about the radiation environment at high altitudes, which will allow aircraft and personnel to avoid locations where health or the mission may be negatively impacted.

15. SUBJECT TERMS
Solar Radiation, Galactic Cosmic Ray, Solar Proton Event, Ground Level Event, Solar Energetic Particles, Radiation Dose Rate, Solar Cosmic Ray, Rigidity, Geomagnetic Cutoff.

16. SECURITY CLASSIFICATION OF:			17. LIMITATION OF ABSTRACT	18. NUMBER OF PAGES	19a. NAME OF RESPONSIBLE PERSON
a. REPORT	b. ABSTRACT	c. THIS PAGE			Christopher G. Smithtro, Maj, USAF (ENP)
U	U	U	UU	109	19b. TELEPHONE NUMBER *(Include area code)* (937) 255-3636, ext 4505